Communications Research Centre

ANALYSIS OF SPACE-BASED RADAR
CLUTTER SPECTRA OVER DIFFERENT
TYPES OF TERRAIN AND THEIR
EFFECTS ON DETECTION PERFORMANCE

by

D. Faubert, B.J. Rook and W. Tam

> **CAUTION**
> The use of this information is permitted subject to recognition of proprietary and patent rights.

CRC REPORT NO. 1408
OTTAWA, NOVEMBER 1986

Gouvernement du Canada
Ministère des Communications

Canadä

COMMUNICATIONS RESEARCH CENTRE

DEPARTMENT OF COMMUNICATIONS
CANADA

ANALYSIS OF SPACE-BASED RADAR CLUTTER SPECTRA
OVER DIFFERENT TYPES OF TERRAIN
AND THEIR EFFECTS ON DETECTION PERFORMANCE

by

D. Faubert, B.J. Rook and W. Tam

(Radar and Communications Technology Branch)

CRC REPORT NO. 1408

November 1986
OTTAWA

TABLE OF CONTENTS

ABSTRACT

A computer model was used to make a detailed analysis of the clutter spectra received by real aperture Space-Based Radars orbiting over different types of terrain. The influence of terrain on L-band SBR detection performance has also been studied. It was found that the clutter spectra tend to become narrower as the grazing angle of the antenna increases but that they broaden as the antenna points progressively more away from the direction of motion of the satellite. The interference caused by the clutter background is progressively higher for ice covered ground but smaller for a snow-covered terrain and the smallest for an ocean background. The minimum detectable velocities of the SBR were found to vary by a factor of up to three according to the terrain type.

1. **INTRODUCTION**

The performance of Space-Based Radar (SBR) surveillance systems depends to a large extent on the microwave radiation backscattered by the terrain over which potential targets are flying. The characteristics of this radar clutter are a function of the parameters of the radar system, the nature of the background terrain and the geometry of the situation.

In previous work carried out at this establishment (Refs. 1-2) a model was developed to investigate the performance of space-based, real aperture, pulse doppler radars. From these studies, a number of parametric relations were derived for the key radar performance figures and a very useful baseline system was established. However, in these studies the surface scattering coefficient was assumed to be independent of the grazing angle of the antenna and of the terrain type over which the targets were flying. For detailed developmental studies of SBRs, a more complete description of clutter and hence the clutter spectra is essential. In this report, we have undertaken the analysis of the clutter spectra as received by an L band real aperture, pulse doppler radar operating from space against targets flying over an ocean background and over snow and ice covered ground. The effect of radar clutter on the detection performance of the system was also investigated.

Sections 2 and 3 of this report describe the SBR and the surface scattering models used in this study. Section 4 gives a detailed description of the clutter spectra received by an SBR for various geometrical arrangements and types of terrain. Section 5 discusses the minimum velocities with which targets can be detected with the baseline SBR studied in this report. Section 6 concludes with a summary of the findings of this work. Finally, an Appendix has been prepared to illustrate how the clutter spectra change when the antenna aperture is weighted to reduce sidelobes.

2. SBR MODEL AND BASELINE SYSTEM

The following is a brief description of the main aspects of the SBR model published in Refs. 1-2, which was the starting point of this work. The material reviewed in this section will be used extensively in the rest of this report. The most important equations will be stated and discussed briefly. The reader is referred to the original publications for more details.

Referring to Fig. 1a, the satellite is assumed to travel along a circular orbit. Its position at an instant of time, t, is given by $\lambda_s(t)$ and $\delta_s(t)$ which are respectively the longitude and the latitude of the satellite with respect to a geocentric coordinate system XYZ rotating with the earth. The North-East-Down (NED) frame of reference is centered at the satellite as shown in Fig. 1b. The antenna is taken to be oriented at an angle ϕ_L (referred to as the azimuth look angle) with respect to the N axis of the NED system and at an angle θ_L (the look down angle) with respect to the NE plane. Fig. 1c shows how θ_L is related to the grazing angle γ_L which is the angle between the line connecting the radar to the target (vector R_0) and a tangent to the surface of the earth where R_0 intersects the earth.
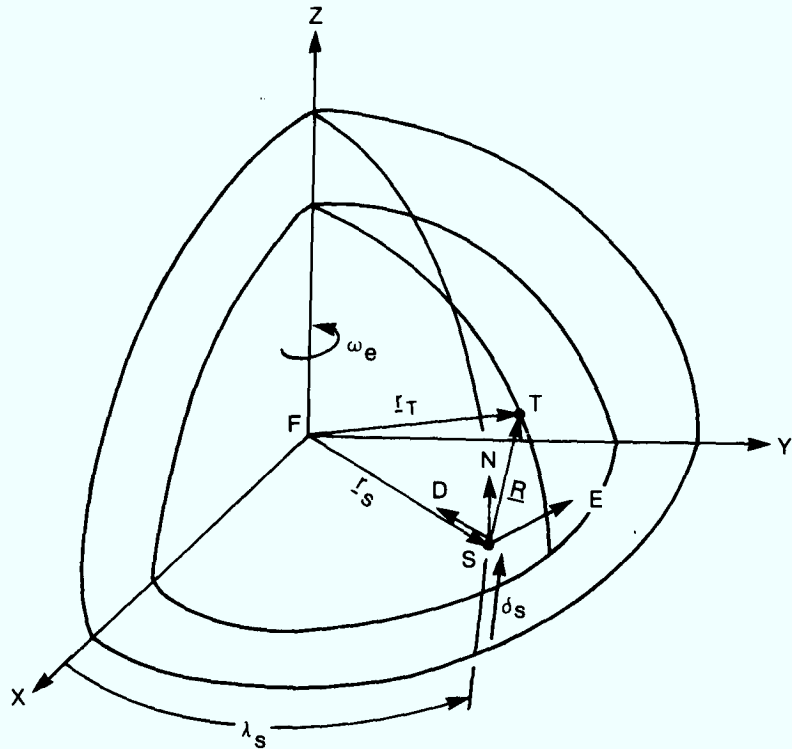

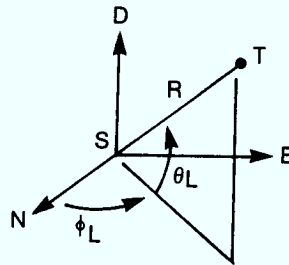Figure 1a - Oribital Configuration for a Space-based Radar

Figure 1b - Orientation of the Radar Antenna in the NED Frame of Reference
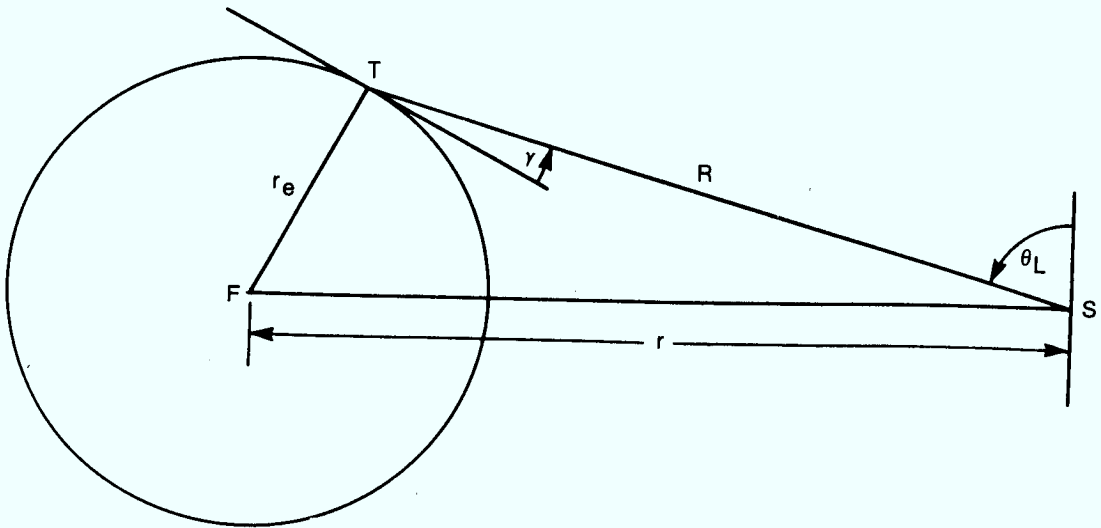
Figure 1c - Relation between the grazing angle (γ_L) and the look-down (ϕ_L) angle of the antenna.

The target is assumed to be flying just above the surface of the earth at a radial velocity (V) with respect to the satellite and is also assumed to be aligned with the axis of symmetry of the antenna (maximum gain). The radar peak power has been chosen to be 17 kW, which is the approximate limit of present day power generation systems on-board spacecrafts. The overall losses (L_s) are set at 9dB. The radar is operating in the L-Band at 1.5 GHz (0.2 m wavelength).

The waveform selected for the pulse Doppler radar is a burst of n pulses with linear frequency modulation. The duty cycle of the pulse train is 0.5. To take advantage of the largest possible coherent integration gain, the value of n is chosen to be:

$$n = \frac{2R_0}{c} \times PRF \qquad [1]$$

where R_0 is the range to the target, c is the speed of light and PRF is the pulse repetition frequency of the waveform. Thus the burst of pulses is chosen to last as long as the time it takes for the radiation to travel back and forth from the surface of the earth after which time the receiver is turned on for an equal length of time. The process is then repeated and it is assumed that two bursts are integrated incoherently to reduce scintillation effects. The PRF is selected to detect unambiguously a certain maximum radial velocity of the target (V_u) with respect to the radar platform:

$$PRF = \frac{4 \ V_u}{\lambda} \qquad [2]$$

In this study, the system is designed to detect a 0.1 m^2 target in noise only, at a maximum range corresponding to a zero degree grazing angle, with a probability of detection of 90% and a false alarm rate of 10^{-6}. Assuming a Swerling Class II target, a 14.8 dB signal-to-noise ratio (SNR) is required for detection under these conditions (Ref. 3). Adding a 3 dB safety margin to account for cusping losses, the detection threshold of the radar is set at 17.8 dB. Thus all the signal parameters in the radar range equation have been determined except for the gain of the antenna which is adjusted through the size of the aperture to obtain the required SNR. The requirement to detect 0.1m^2 targets results in a rather large antenna size of 70 m (projected to be achievable in the future (Ref. 4)). Table 1 summarizes the values used for the radar systems.

TABLE 1

Altitude of satellite (h)	1000 km
Velocity of satellite	7.35 km/s
Radar peak power (P_k)	17 kW
Antenna diameter (D)	70.0 m
Wavelength (λ)	0.2 m
Pulse repetition frequency (PRF)	10 kHz
Pulse length before compression (c)	50 μs
Compression ratio (C_0)	0.0122
System temperature (T_s)	490°K
System losses (L_s)	9 dB
Probability of detection (P_D)	90%
False alarm rate (FAR)	10^{-6}
Target model	Swerling II
Target cross section (σ_t)	0.1 m^2
Altitude of target	0.0 km
Radar maximum range	3709 km

Thus the strength of the signal received from the target is calculated using the standard radar range equation:

$$S = \frac{n^2 \, P_K \, \tau \, G^2 \lambda^2 \, \sigma_t}{(4\pi)^3 \, R^4 L_s} \qquad [3]$$

and the system noise level is given by:

$$N = n \, k \, T_s \qquad [4]$$

where k is the Boltzman constant.

It is well known that a waveform consisting of a burst of pulses gives rise to ambiguities in the measurement of range. In our problem this results in a series of circles on the surface of the earth (Fig. 2) for which the range from the transmitter to any point on the ith circle is constant and is given by:

$$R_i = R_o \pm i \, \frac{c}{2PRF} \qquad i = 0, \pm 1, \pm 2 \, ... \qquad [5]$$
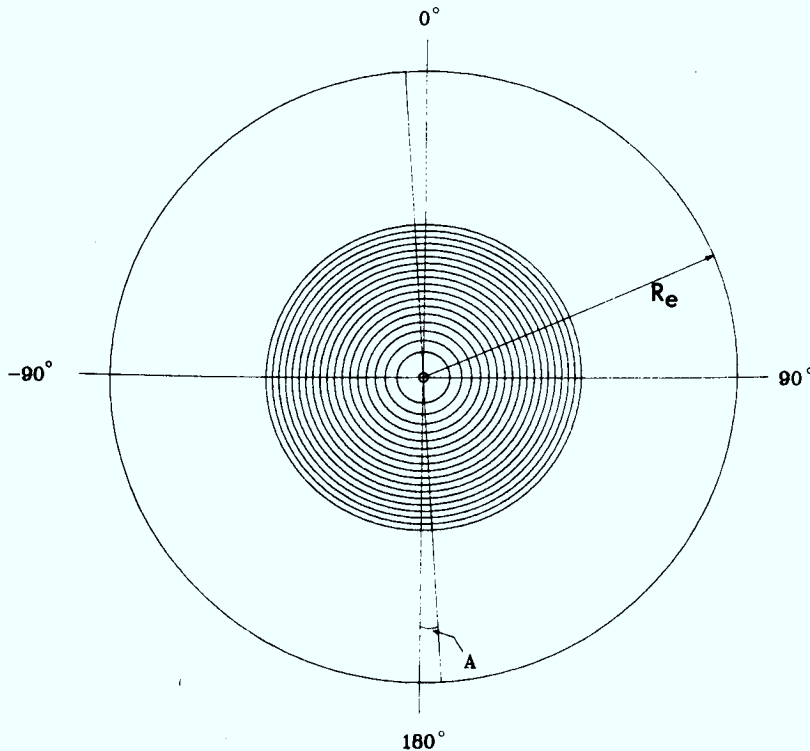

Figure 2 – Ambiguous range circles on the surface of the Earth as seen from infinity along a line connecting the satellite and the center of the earth. The outer circle is the contour of the earth. Since one range line out of ten is plotted in this drawing, the main range line (i=0) lies in the vicinity of the second outermost circle.

Note that in this report, these circles of constant range to the transmitter will be interchangeably referred to as range circles, range rings or range lines.

In Eq. 5, R_0 is the range to the surface of the earth along the primary look direction of the antenna. This range circle, i equals 0, is referred to as the primary or main range circle. Because the target is assumed to be boresighted with the radar antenna and to fly very close to the surface of the earth, R_0 is also the range from the radar to the target.

For each range circle the grazing angle γ_i is defined as the angle between R_i and a tangent to the surface of the earth at the point where R_i intersects the surface of the earth. The positive range line numbers (i>o) are assigned to those rings located beyond the main range line ($R_i > R_0$), and they will number from one to m such that γ_m is the smallest possible angle larger or equal to zero. Conversely, the negative range line numbers (i < o) are assigned to those range lines located below R_0 ($R_i < R_0$) which are ranging from -1 to -m' such that $\gamma_{-m'}$ equals to the largest angle smaller than or equal to 90°. The total number of ambiguous range circles depends on the altitude of the satellite, the PRF of the radar and the number of pulses in the burst while the relative number of positive and negative range lines depends however on the grazing angle at which the antenna is pointing (γ_0). The larger γ_0, the larger the total number of positive range lines and the fewer the number of the negative ones.

All the clutter elements located on these ambiguous range circles are contributing power to the clutter spectrum. It was shown in Refs. 1-2 that the clutter spectrum (energy) can be calculated from the following equation:

$$C(V) = \frac{P_K \ \tau \ G^2 \ \lambda^2}{(4\pi)^3 L_s} \sum_{i=-m'}^{m} \frac{W_i^2}{R_i^4} \left(\frac{c \ \tau C_0 \ R_i \ \cos \theta_i \ \Delta\phi}{2 \cos \gamma_i} \right) \sigma_0(\gamma_i) G^2(\theta_i, \phi_i)$$

[6]

where V is the radial velocity of the clutter elements with respect to the radar corresponding to a Doppler shift:

$$f_d = \frac{2V}{\lambda}$$

[7]

The summation in Eq. 6 takes into account the clutter power contributed by the scatterers located on each ambiguous range line. The term in parenthesis in Eq. 6 is the area on the surface of the earth corresponding to one compressed range resolution cell (ΔR) of the radar:

$$\Delta R = \frac{cC_o\, \tau}{2} \qquad [8]$$

where C_o is the compression factor of the waveform. The value of this elemental area is multiplied by the surface scattering coefficient $\sigma_o(\gamma_i)$ of the terrain to obtain the effective cross section of the clutter element. Note that in Eq. 6 $\Delta\phi$ refers to the extent in azimuth of a single clutter element.

The weights W_i in Eq. 6 account for the fact that some pulses within the burst may arrive either too early or too late with respect to the opening time of the receiver to be coherently integrated. These weights are given by

$$W_i = n - |i| \qquad \text{for } |i| < n$$
$$= 0 \qquad \text{otherwise} \qquad [9]$$

Finally, the term $G(\theta_i, \phi_i)$ is the gain of the antenna in the direction of the scatterer located at an azimuth angle ϕ_i on the ith ambiguous range line. As shown in Ref. 1-2

$$\phi_i = \cos^{-1}\left[\frac{V}{V_{MAX}(i)}\right] - A \qquad [10]$$

with

$$V_{MAX}(i) = \cos\gamma_i\left((V_{gs}\cos\Delta)^2 + (V_e\cos\delta_s - V_{gs}\sin\Delta)^2\right)^{\frac{1}{2}} \qquad [11]$$

$$A = tg^{-1}\left[\frac{V_e\cos\delta_s - V_{gs}\sin\Delta}{V_{gs}\cos\Delta}\right] \qquad [12]$$

and where

$$V_e = R_e\,\omega_e \qquad [13]$$
$$V_{gs} = R_e\,\omega_s \qquad [14]$$

$$\Delta = \cos^{-1}\left[\pm\frac{\cos u \sin I}{(1-\sin^2 u \sin^2 I)^{\frac{1}{2}}}\right] \qquad [15]$$
$$u = w + f \qquad [16]$$

In these equations, ω_e and ω_s are the angular velocities of the earth and the satellite R_e is the radius of the earth, I is the inclination

angle of the orbital plane with respect to the equatorial plane of the earth and the angles w and f are respectively the argument of the pericenter of the orbit and the true anomaly of the satellite (Refs. 1-2). For a polar orbit, which is of interest here, I and Δ equal 90° and we have:

$$V_{MAX}(i) = \cos\gamma_i\left((Vgs)^2 + (V_e \cos\delta_s)^2\right)^{\frac{1}{2}} \qquad [17]$$

$$A = tg^{-1}\left[\frac{V_e \cos\delta_s}{V_{gs}}\right] \qquad [18]$$

Because of the finite length of the pulse burst T_B, the Doppler resolution of the processor is limited to a velocity bin width, ΔV, given by:

$$\Delta V = \frac{\lambda}{2T_B} \qquad [19]$$

Thus in order to compute the total amount of clutter energy contributing to a velocity bin centered on V, Eq. 6 has to be applied to all speeds within the interval $[V-\Delta V/2, V+\Delta V/2]$ and the corresponding C(V) summed:

$$C_V = \sum_{V \in \Delta V} C(V) \qquad [20]$$

Finally, the signal-to-interference ratio (SIR) which will be used as a measure of the detection capability of the system is given by:

$$SIR(V) = \frac{S}{N + C_V} \qquad [21]$$

From this last equation it is seen that when the clutter energy at a certain velocity is negligible, the system is noise limited and SIR(V) reduces to the signal-to-noise ratio, SNR, of the system. On the other hand, when the noise is much smaller than the clutter signal, the system is said to be clutter limited and SIR(V) reduces to the signal to-clutter ratio, SCR(V).

3. SURFACE SCATTERING MODELS

In order to understand the influence of terrain type on SBR operation, we have selected three different clutter models for which the dependences of the surface scattering coefficient (σ_o) versus the grazing angle are shown in Fig. 3. They are:

a) Sea model (HH polarization, Ref. 5, corresponding approximately to a Sea State 3 condition).

b) Snow model (HH polarization, Ref. 6). These experimental data were collected for a 58 cm snow depth. Since snow is to a large extent transparent for L-Band radiation, this model can also be taken to describe the backscattering characteristics of the underlying terrain (ground covered with short vegetation in this case).

c) Ice model (VV polarization, Ref. 7). These measurements were taken over thick (2-3 m) multi-year sea ice.
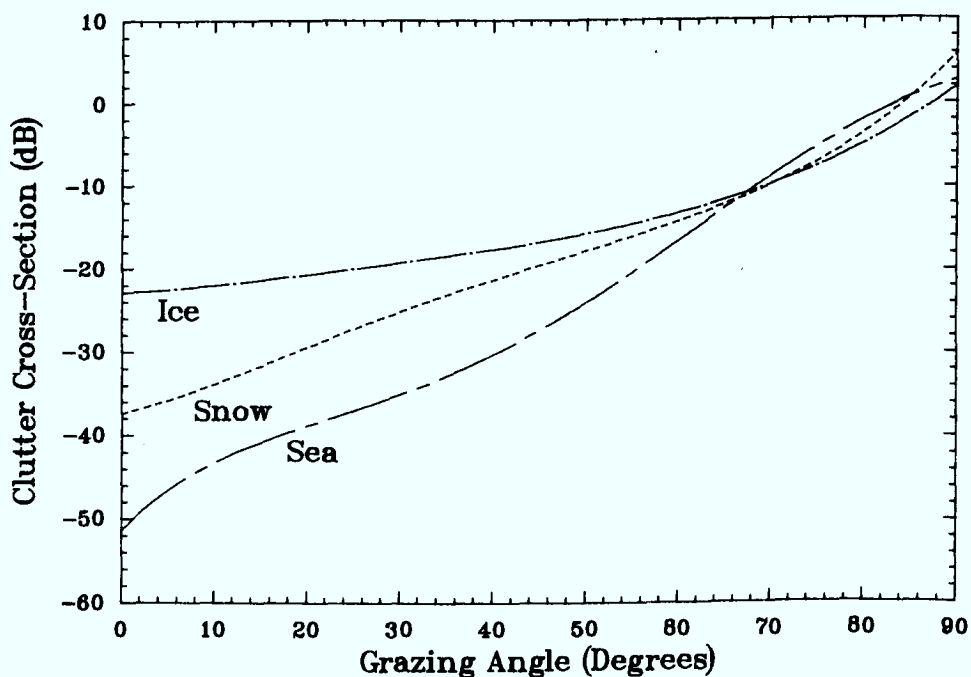

Figure 3 - Surface backscattering models used throughout this study

The specific models used in this report were retained after a survey of the cross-section data available in the open literature. These types of terrain were selected because of their relevance to SBR surveillance over the Canadian Arctic and because they span a fairly broad range of values of σ_O as the grazing angle varies.

As experimental data for low and high grazing angles are not readily available, the data for the three curves of Fig. 3 were first extra-

polated to γ=0° and γ=90° and were then fitted with power series in γ to facilitate the numerical evaluation of $\sigma_o(\gamma)$. The resulting polynomials are:

$$\sigma^o_{ocean} = -51.371 + 65.661x - 142.09x^2 + 193.24x^3 - 102.08x^4 \qquad [22]$$
$$+ 18.199x^5$$

$$\sigma^o_{snow} = -37.4 + 15.887x + 31.779x^2 - 42.481x^3 + 17.156x^4 \qquad [23]$$

$$\sigma^o_{ice} = -22.876 + 2.7357x + 13.813x^2 - 14.397x^3 \qquad [24]$$
$$+ 6.9247x^4$$

where the σ^o are in dB and x is the grazing angle in radians.

4.   CLUTTER SPECTRA

The clutter spectra detected by the SBR system described in the previous pages and their corresponding SIR curves are analyzed in detail in this section. The results are used to describe the capability of an SBR to detect slow moving targets in the presence of heavy earth clutter (Section 5). Unless otherwise specified, the satellite is in a polar orbit (I = 90°) and is located above the equator when the clutter spectrum is recorded ($\delta s = 0°$).

4.1   Clutter Spectrum of the Baseline System at Low Grazing Angle

In this first example, the radar antenna is pointed at a very low grazing angle ($\gamma_L = 3°$) and is aligned with the direction of motion of the satellite ($\phi_L = 0°$) and the clutter model is for the ocean. Fig. 4 shows a three dimensional plot of the clutter power as a function of the radial speed of the scatterers relative to the satellite and as a function of the range line number. Note that in this example, there is a total of 181 range lines out of which 21 are located at a grazing angle smaller than 3° (positive i) and 159 at a grazing angle of larger than 3° (negative i). Fig. 5 shows the resulting clutter spectrum when the clutter power from each range line are added together. The power scale is logarithmic (i.e. in dB) to highlight the large variations of the clutter power as a function of both V and i.

The numbers on the upper axis in Fig. 5 are the radial velocities (V_A) of the clutter elements with respect to the satellite. The lower axis on the other hand is referred to as the relative radial velocity axis and the values are denoted by V_R. V_R is chosen to be zero for the scattering element boresighted with the radar antenna. Its corresponding speed on the V_A axis is denoted by V_O (V_O = 6345.3 m/s in this example). Because the whole spectrum is shifted by $2V_O/\lambda$ from the carrier frequency of the radar and V_O varies with γ_L and ϕ_L, the use of the relative velocity V_R scale makes it much easier to compare clutter spectrum for different orientations of the antenna. Also V_R may be
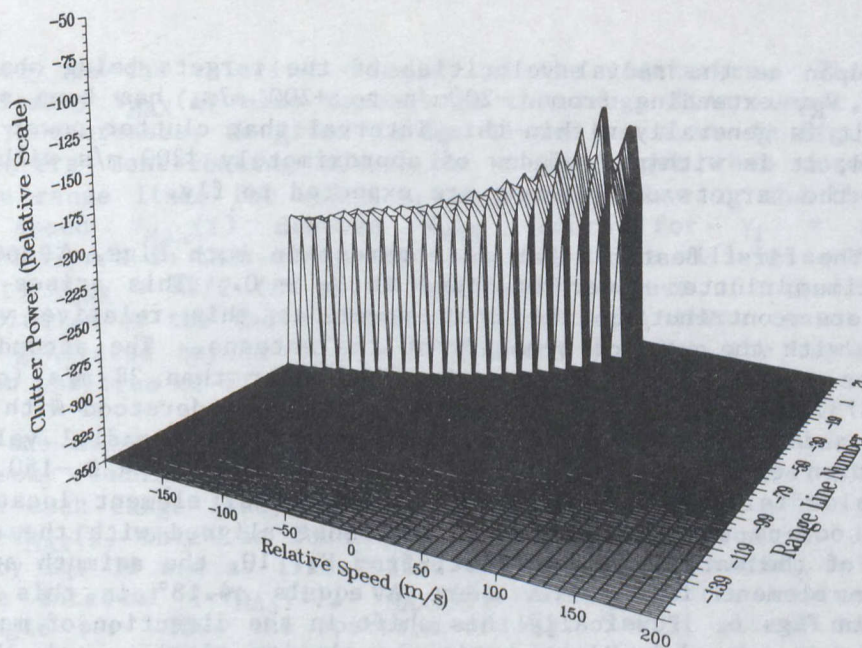
Figure 4 — Three-dimensional clutter spectrum for the baseline system at low grazing angle ($\gamma_L=3°$, $\phi_L=0°$)
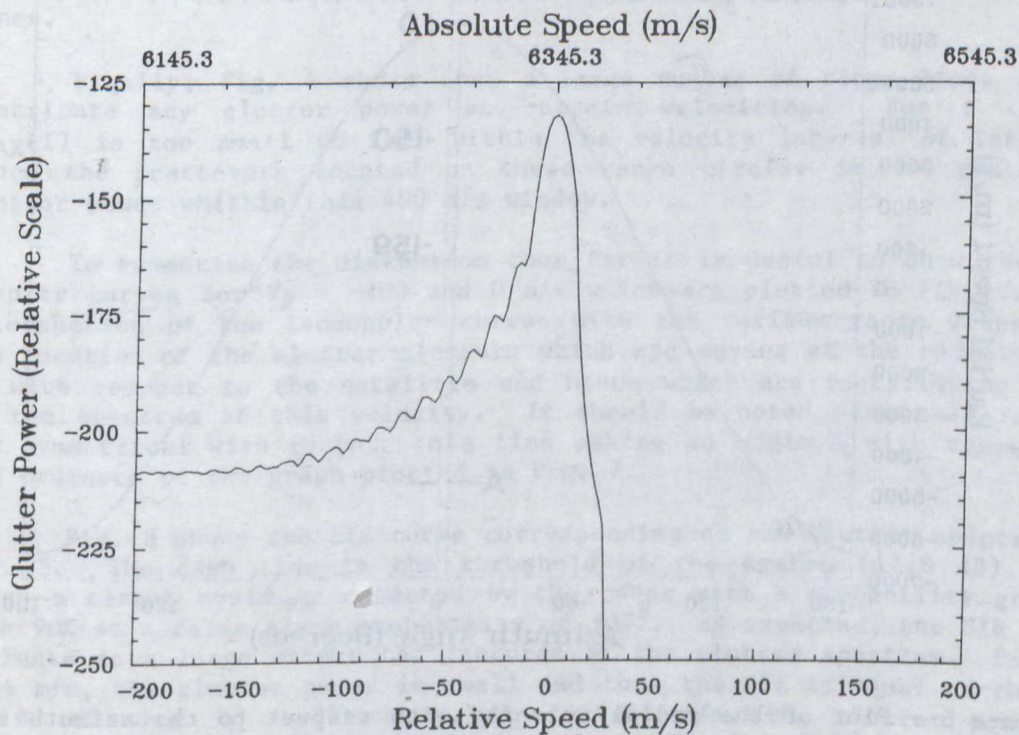

Figure 5 — Clutter spectrum for the baseline system at low grazing angle ($\gamma_L=3°$, $\phi_L=0°$)

looked upon as the radial velocities of the targets being observed. The span of V_R, extending from −200m/s to +200 m/s, has been selected because, it is generally within this interval that clutter power is significant and, it is within a window of approximately ±200 m/s with respect to V_o that the targets of interest are expected to fly.

The first feature that is apparent in both Figs. 4 and 5 is that the maximum clutter power is found at $V_R = 0$. This arises because the scatterers contributing the most power at this relative velocity are aligned with the axis of symmetry of the antenna. The second feature is that the clutter power is zero for V_R larger than 28 m/s (or V_A larger than 6373.19 m/s). The reason for this can be understood with the help of Eq. 10 and Fig. 6, the latter being a graph of the radial velocity V_A as a function of ϕ for three different range lines (i = 0,−150,−159). The maximum radial velocity $V_{MAX}(i)$ of any clutter element located on range line i occurs when its position is almost aligned with the direction of motion of the satellite. In fact, from Eq. 10, the azimuth angle of this clutter element is $\phi_i = A$ where A equals +4.18° in this example, as shown in Fig. 6. Physically this shift in the direction of maximum radial velocity is caused by the rotational velocity of the earth which is con−
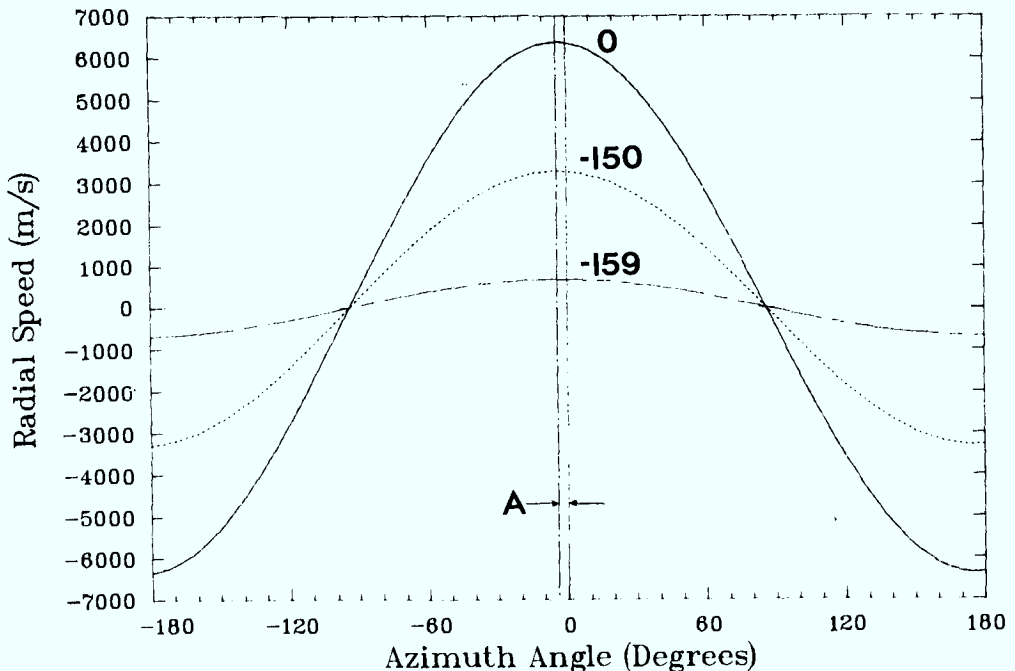

Figure 6 − Plot of the radial velocity with respect to the azimuth angle, for three different range circles. Similar curves for i > 0 overlap the one for i = 0. The grazing angles γ_i corresponding to the range lines 0,−150 and −159 are respectively 3°, 58.93° and 83.79°.

ing slightly to the relative velocity of the scatterers. This maximum radial velocity $V_{MAX}(i)$ also depends on the range line number, decreasing when γ_i increases, as given in Eq. 11 and as shown in Fig. 6. Thus the scatterers contributing power for a V_R larger than zero will be located on range lines for which γ_i is smaller than γ_L and the largest possible speed $V_{MAX}(i)$ denoted V_{MAX} occurs for $\gamma_i \simeq 0°$ (V_{MAX} equals 6370.97 m/s in this example). Actually there will be some power at V_A equal to $V_{MAX} + \Delta V/2$ ($\Delta V = 4.42$ m/s here) because of the finite velocity resolution of the radar waveform. Therefore, there cannot be clutter power generated beyond $V_{MAX} + \Delta V/2$ which explains the rapid drop in the clutter spectrum of Fig. 5.

On the negative side of the V_R axis the clutter spectrum decreases with some undulations. Since there is a maximum relative speed $V_{MAX}(i)$ on each range line, there is from symmetry also a minimum speed equal to $-V_{MAX}(i)$ which is found in the direction ϕ equal to $180° + A$. As given by Eq. 10 and as illustrated in Fig. 6, the radial velocity V_A within the interval $[-V_{MAX}(i), V_{MAX}(i)]$ varies as the cosine of the azimuth angle ϕ_i. Thus the spectrum of Fig. 5 will extend down to V_R equals $-V_{MAX}(i) - \Delta V/2$ decreasing in amplitude as the gain of the antenna decreases away from the antenna boresight. Note however that we are only interested in a small portion of the total interval extending from 6145.3 to 6545.3 m/s. The undulations are caused by the gain of the antenna pattern which is not uniform and by the spacing between the range lines.

Finally, Fig. 4 shows that a large number of range lines do not contribute any clutter power at certain velocities. For $i < -60$, $V_{MAX}(i)$ is too small to fall within the velocity interval of interest. Hence the scatterers located on these range circles do not contribute clutter power whithin this 400 m/s window.

To summarize the discussion thus far it is useful to show the isodoppler curves for $V_R = -200$ and 0 m/s which are plotted in Fig. 7. The intersection of the isodoppler curves with the various range lines give the location of the clutter elements which are moving at the radial speed V_R with respect to the satellite and hence which are contributing power to the spectrum at this velocity. It should be noted that all isodops are symmetrical with respect to a line making an angle A with respect to the ordinate of the graph plotted in Fig. 7.

Fig. 8 shows the SIR curve corresponding to the clutter spectrum of Fig. 5. The dash line is the threshold of the system (17.8 dB) above which a target would be detected by the radar with a probability greater than 90% at a false alarm probability of 10^{-6}. As expected, the SIR curve reflects to a large extent the features of the clutter spectrum. For $V_R > 14$ m/s, the clutter power is small and thus the SIR is equal to the SNR (19.02 dB when $\gamma_L = 3°$). For $V_R < -40$ m/s, the clutter power is small and the SIR approximately equals the SNR. For $V_R = 0$ m/s the SIR equals, to a good approximation, the SCR (-26.73 dB) since the clutter power is much larger than the noise. With this geometry, it would prove
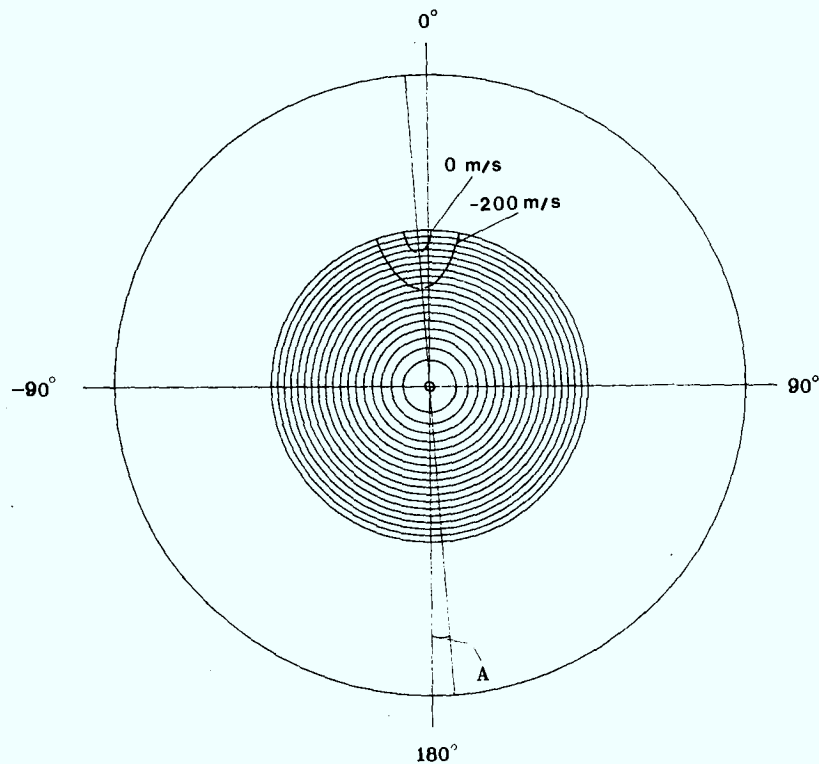
Figure 7 - Isodoppler curves for the baseline system at low
grazing angles ($\gamma_L=3°$, $\phi_L=0°$)

relatively easy to detect targets approaching the radar at a V_R greater
than approximately +14 m/s but receding targets would not be detected
unless they travel at least as fast as -40 m/s. The minimum detectable
velocities (MDV) of the system (-40 m/s and 14 m/s for the baseline sys-
tem) are defined as the minimum values of the approaching (positive MDV)
and the receding (negative MDV) radial velocities of the target above
which the SIR of the radar is always above the detection threshold. These
MDV's are one measure of the detection performance of an SBR and will be
discussed at length in Section 5.

4.2   Effect of Terrain

Fig. 9 shows the SIR curves for the various types of clutter models
described in Sect. 3.   The clutter is largest for ice covered ground
followed by snow covered terrain and then the ocean background. It can be
seen that the differences in the SIR values at V_R equals 0 m/s for the
various terrains are approximately equal to the differences in the clutter
cross sections for the grazing angle at which the antenna is pointing (3°
here) as can be verified with the help of Fig. 3.   This is reasonable
because the clutter elements contributing the most power at V_R equals 0
m/s are those boresighted with the antenna axis.   For $V_R \neq 0$ m/s, the
clutter power also changes as a function of the type of terrain since the

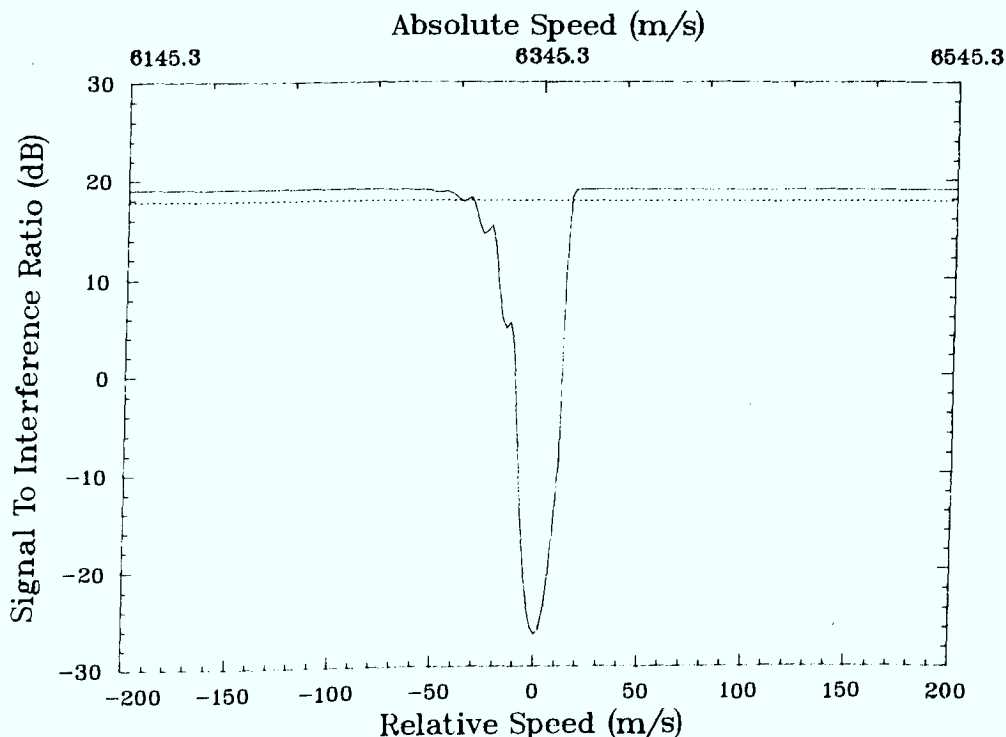cross section of the contributing scatterers is a function of their respective γ_i.

Figure 8 – SIR curve for the baseline system at low grazing angle ($\gamma_L=3°$, $\phi_L=0°$)

The impact of terrain on the MDVs of an SBR is clearly illustrated in Fig. 9. They range from [-40 m/s, 14 m/s] for the ocean model to [-108 m/s, 22 m/s] for ice. The detailed analysis of the effect of terrain on the MDVs of an SBR is postponed until Section 5.0. Until then, we will concentrate on the analysis of the clutter spectra for different geometries in order to develop the concepts necessary to analyze the performance curves presented in Section 5. In view of the similarity in the shape of the SIR curves for different terrain, we will concentrate our analysis on the ocean background. We will return to the other types of terrain in Section 5.

4.3   Effect of the Latitude of the Satellite

The clutter spectrum of an SBR changes only slightly when the latitude of the satellite changes. Fig. 10 shows the SIR curve for δ_s equals 90° (the satellite is located over the north pole) superposed over that for δ_s equal to 0°, all other parameters being identical.

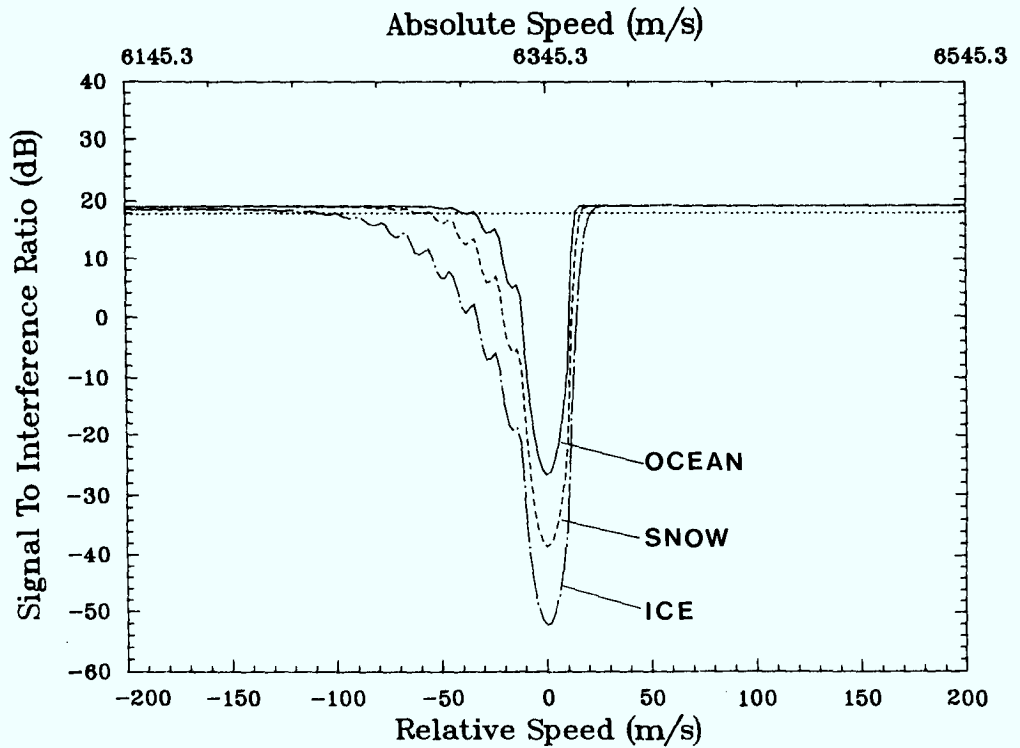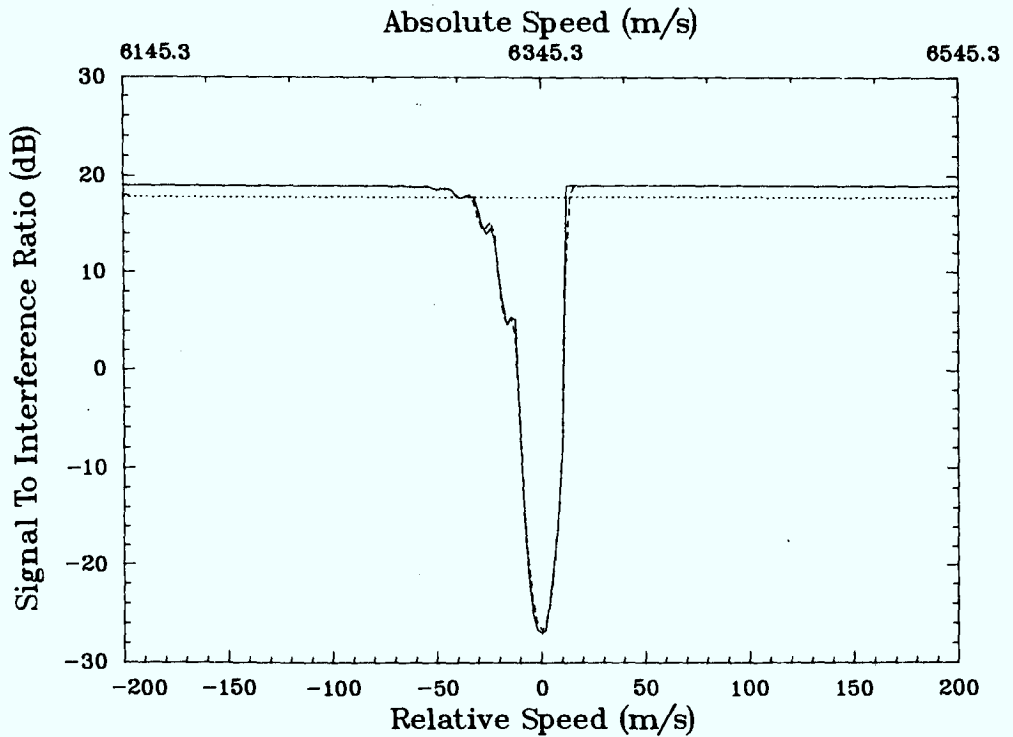Figure 9 – Effect of terrain on the SIR of the SBR ($\gamma_L=3°$, $\phi_L=0°$)

Figure 10 – Effect of the latitude of the satellite on the SIR of the baseline system ($\gamma_L=3°$, $\phi_L=0°$). The continuous curve is for $\delta_s=0°$ and the dashed curve for $\delta_s=90°$.

The two curves are very similar except that the δ_s equals 90° curve is somewhat sharper on the positive side of the relative velocity axis. From this position in space, any point on the surface of the earth moves in a direction which is normal to the vector joining the radar to that point. Consequently the rotation of the earth does not contribute to the radial velocity of the clutter element. This results in a somewhat smaller maximum radial velocity (as per Eq. 17) which shows up quite clearly on the positive side of the spectrum. Eq. 12 shows that the angle A equals zero when δ_s equals 90° which confirms the fact that from this view point in space, the rotation of the earth does not affect the clutter spectrum. Since changing δ_s has only a small effect on the clutter spectrum only δ_s equals zero will be considered in the rest of this report.

4.4   Effect of the Inclination Angle of the Orbit of the Satellite

When the inclination angle, I, of the orbit varies, some changes in the clutter spectrum and hence in the signal-to-interference curve occur. Fig. 11 compares the SIR curves for an equatorial orbit and for a polar orbit. It should be noted that in both cases the satellites are located at the same point in space (above the Greenwhich meridian) but are moving in different directions.

The upper axis of Fig. 11 shows V_o for the equatorial orbit and is smaller than that for the polar orbit (5880.8 m/s as compared to 6345.3 m/s).This is because in this geometry the angular velocity of the satellite is in the same direction as that of the earth. Eq. 12 shows that the angle A equals 90° here which indicates that the maximum radial velocity of the clutter elements with respect to the radar occurs in a direction which is aligned with the direction of motion of the satellite. It should be noted that in this geometry the N axis of the NED system is normal to the direction of motion of the satellite whereas for I = 90°, it was aligned with it.

Fig. 11 shows that the relative radial velocity at which the clutter power is small ($C_V \approx 0$) occurs at ≈ 12 m/s for the equatorial orbit, as compared to ≈ 14 m/s for the polar orbit. This arises because the largest relative velocity $V_{MAX}(i)$ on any range line occurs for the clutter elements which are aligned with the direction of motion of the satellite for an equatorial orbit. This difference in $V_{MAX} - V_o$ can be understood with the help of Eq. 10. By definition of V_{MAX} (V_{MAX} occurs on the range line closest to the horizon which is i=21 here) and V_o, we have:

$$V_{MAX} - V_o = V_{MAX}(i=21) - V_{MAX}(i=0) \cos(\phi_L + A) \qquad [25]$$

thus

$$V_{MAX} - V_o = \left((V_{gs}\sin\Delta)^2 + (V_e\cos\delta_s - V_{gs}\cos\Delta)^2 \right) \times \left(\cos\gamma_{21} - \cos\gamma_o\cos(\phi_L + A) \right)$$

$$[26]$$

The values of the factors within the first and the second brackets of Eq. 26 are both smaller for the equatorial orbit than for the polar. This explains the small decrease in the minimum value of the approaching velocity of a target that the SBR can detect on the equatorial orbit.
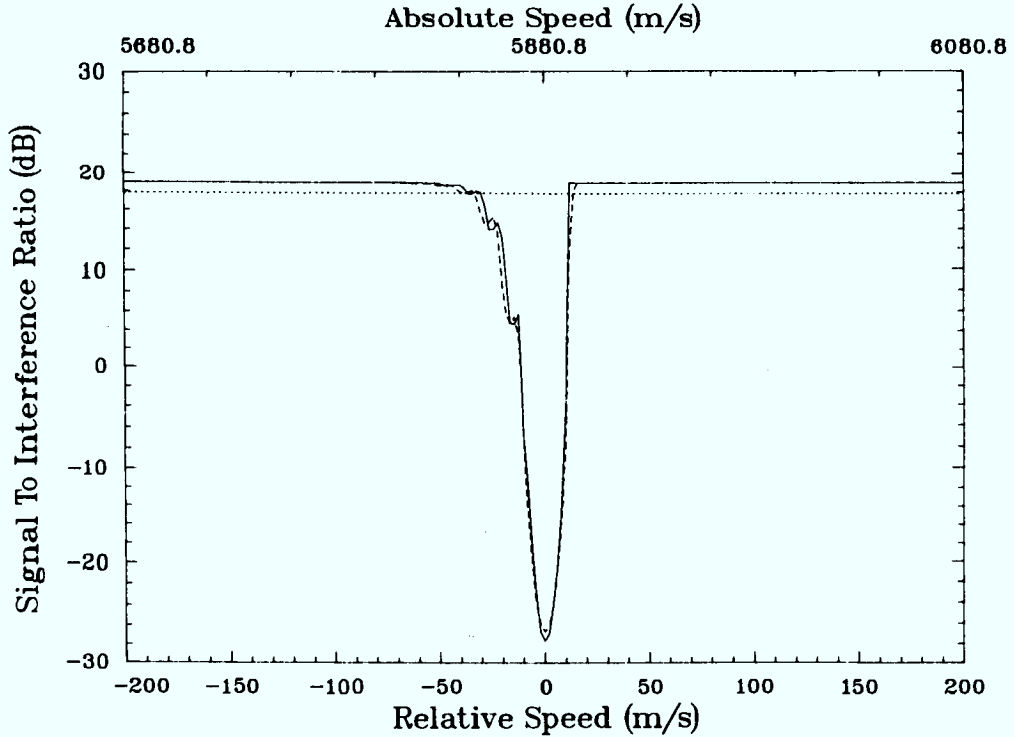

Figure 11 - Effect of the inclination angle of the orbit of the satellite on the SIR of the baseline system ($\gamma_L=3°$, $\phi_L=0°$). The dashed curve is for the polar orbit (I=90°) and the continuous curve is for the equatorial orbit (I=0°).

Finally, Fig. 11 indicates that for V_R equals 0 m/s, the SIR is slightly larger for the equatorial than the polar orbit (by approximately 0.25 dB). Although this effect is small, it is explained as follows. The total amount of power at a certain relative velocity V_R is the sum of all clutter power of the scatterers located within a certain velocity bin width (Eq. 20). On a given range line, these scatterers will be found within two intervals of extent $\Delta \phi$ located symmetrically on either side of A:

$$\Delta \phi_T = \left[\phi_{V_R-\Delta V/2}, \ \phi_{V_R+\Delta V/2} \right] \qquad [27]$$

where $\phi_{V_R} \pm \Delta V/2$ are related to $V_R \pm \Delta V/2$ through Eq. 10. Thus because $VMAX_i$ is slightly smaller for the equatorial orbit as compared to

the polar case, it can be shown that $\Delta\phi_T$ will be slightly wider for the former (by approximately 0.05°). Consequently, the area of terrain contributing power to the clutter spectrum at $V_R = 0$ is slightly larger for equatorial orbits, which results in a somewhat larger clutter power.

Since the effects described above are rather small, only data pertaining to polar orbits will be presented in the remainder of this work.

4.5   Effect of the Azimuth Look Angle of the Antenna

In this section the radar antenna is still pointed at a low grazing angle ($\gamma_L = 3°$) but is now oriented in a direction which is normal to the direction of motion of the satellite. Fig. 12 shows the resulting three dimensional clutter spectrum. Fig. 13 is the corresponding two-dimensional clutter spectrum with the ϕ_L equals 0° also shown (dashed line) for comparison.

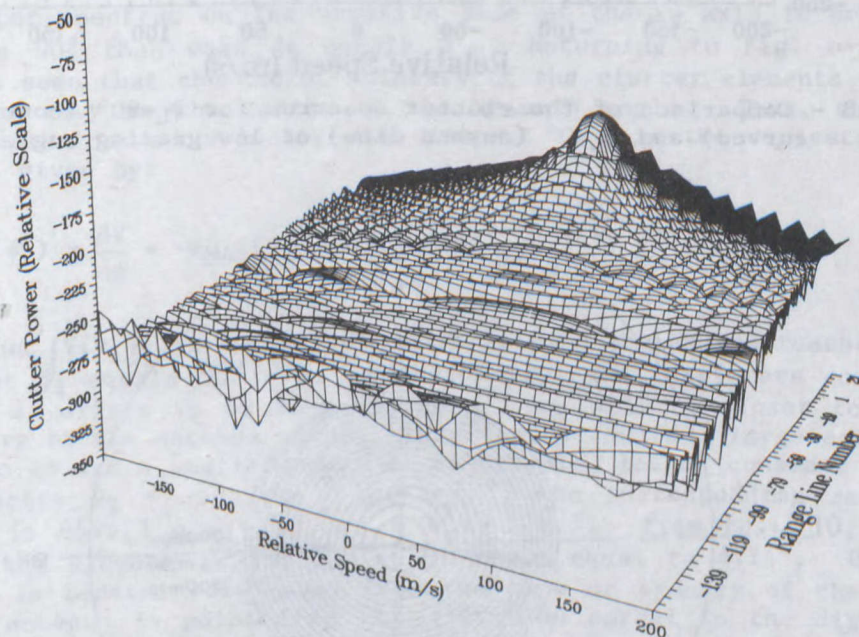Figure 12 – Three-dimensional clutter spectrum on the baseline system for $\phi_L=90°$ ($\gamma_L=3°$)

It is observed from Fig. 13 that V_O is very small ($V_O = -464.47$ m/s which is equal to the velocity of the earth at the equator) as compared with the $\phi_L = 0°$ situation ($V_O = 6345.3$ m/s). This is because the antenna is pointed in a direction which is normal to the direction of motion of the satellite. However, V_O is not equal to 0 m/s since the radial velocity vanishes at 90° from angle A (+4.18°) as seen from Eq. 10
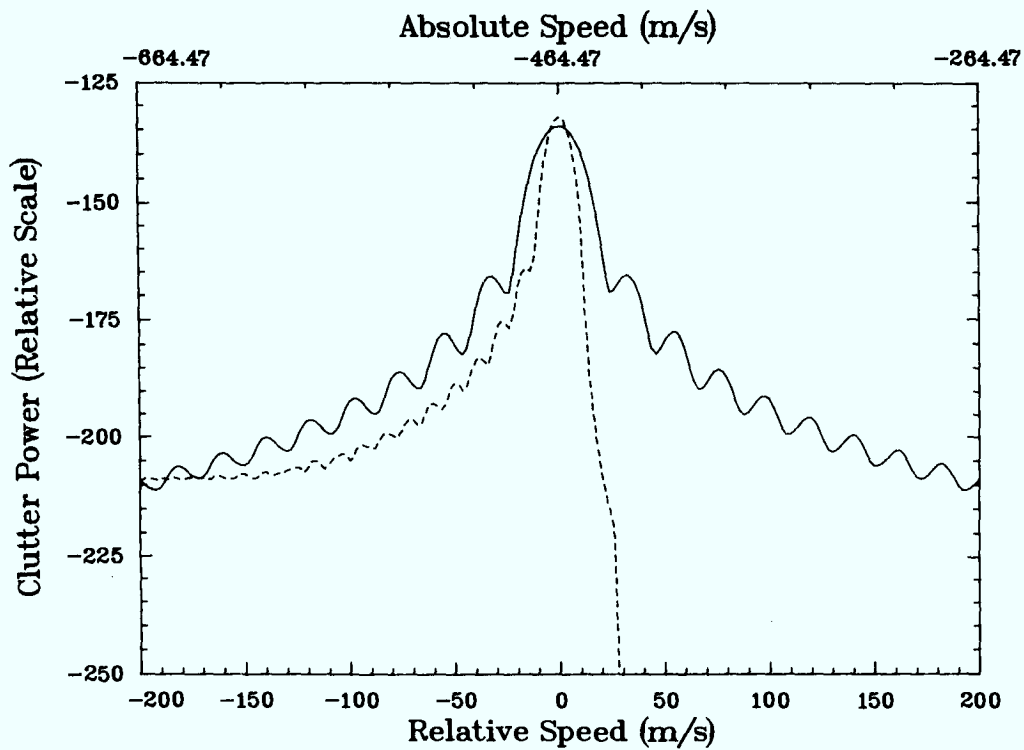
Figure 13 - Comparison of the clutter spectrum for $\phi_L=90°$ (continuous curved) and $\phi_L=0°$ (dashed line) at low grazing angle $\gamma_L=3°$)
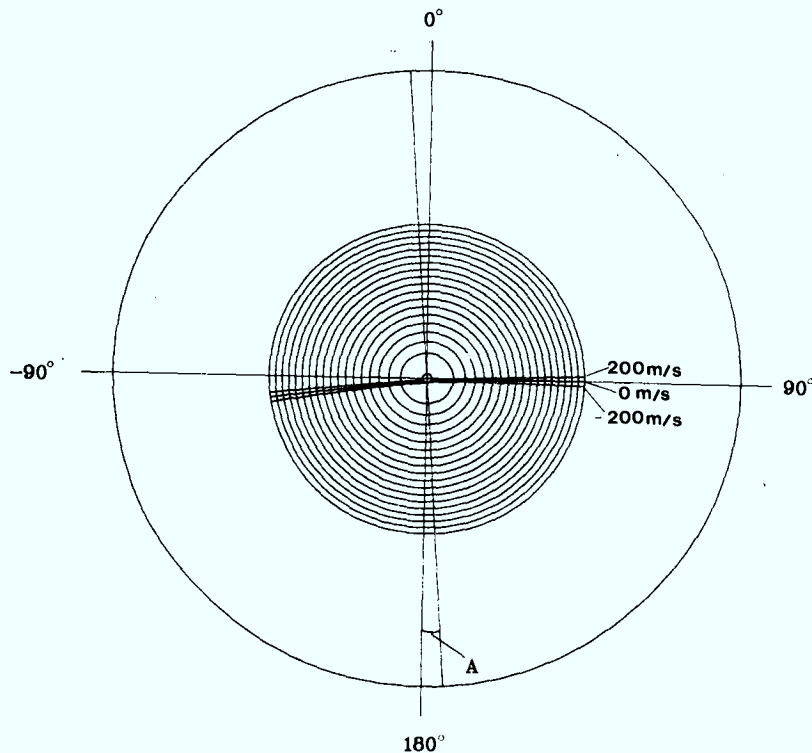

Figure 14 - Isodops for the baseline system when $\phi_L=90°$ ($\gamma_L=3°$)

and as shown in Fig. 6. Thus V_O would be zero for ϕ_L equals 85.82 degrees and here V_O is negative because it is located at 94.18 degrees with respect to the angle A. Fig. 14 shows the isodops for V_R equals -200, 0 and 200 m/s respectively. For these relative velocities most of the clutter elements contributing to the spectrum are actually moving away with respect to the spacecraft.

As in Section 4.1, the clutter spectrum still extends from [-6373.19 m/s, 6373.19 m/s] since this interval does not depend on the azimuth angle of the antenna. The spectrum is nearly symmetrical with respect to $V_R = 0$ because V_O is almost zero. It would be perfectly symmetrical with respect to this point only if the antenna were pointed in a direction normal to the direction of maximum radial velocity i.e. perpendicular to A ($\phi_L = 85.82°$ in this example). One of the practical consequences of this wide clutter spectrum is that the clear area on the positive relative velocities axis observed for $\phi_L = 0°$ has disappeared, making the detection as difficult for approaching as for receding targets.

There are two more rather subtle features shown in Fig. 13. First the clutter spectrum on the negative side of the V_R axis is broader when ϕ_L equals 90° than when ϕ_L equals 0°. Returning to Fig. 6 or to Eq. 10, it is seen that the radial velocity of the clutter elements on a given range line vary as the cosine of the azimuth angle. Thus, the rate of change of the radial velocity with respect to ϕ is the derivative of Eq. 10 and is given by:

$$\dot{V}(\phi_i) = \frac{dV}{d\phi} = -V_{MAX}(i) \sin(\phi_i + A) \qquad [28]$$

Thus $\left| \dot{V}(\phi_i) \right|$ is smaller at small azimuth angles and reaches a maximum at ϕ_i equals 90° - A. Consequently, the scatterers contributing power at a certain V_R on a given range line will be closer to the axis of symmetry of the antenna when it is oriented toward a large azimuth look angle than toward a smaller one. As an example, let us consider the relative velocity $V_R = -50$ m/s. For $\phi_L = 0°$, the corresponding radial velocity V_A is 6545.3 m/s – 50 m/s = 6295.3 m/s. From Eq. 10, for i=0, this clutter element is located at an angle equal to 4.14°. Hence this scatterer is located 4.14° away from the axis of symetry of the antenna. When the antenna is pointed in a direction normal to the direction of motion of the satellite, ($\phi_L = 90°$), the corresponding numbers are: V_A = -464.47 m/s -50 m/s = -514.47 m/s, ϕ = 90.5°. Hence, the clutter element is located only 0.5 away from the direction of antenna boresight. Since the gain of the antenna is larger for the sidelobes which are closer to the mainlobe, the clutter power at a given V_R is larger when ϕ_L is equal to 90° than when equal to 0°, which of course results in a broader spectrum, as observed in Fig. 13.

The second feature of Fig. 13 is the larger amount of clutter (≈ 2 dB) at V_R equals 0 m/s when the antenna is pointed in the direction of

motion of the spacecraft (ϕ_L =0°). This appears to contradict the con-
clusion which was just reached but also arises from Eq. 28. Eq.27 indi-
cates that the total amount of power at a certain relative velocity V_R
is produced by clutter patches located within two azimuth intervals
defined by $\Delta\phi_T$. Thus from Eq. 28 since $\dot{V}(\phi)$ is larger at larger azimuth
angle, the extent of the interval $\Delta\phi_T$ is smaller at ϕ_L equals 90° than
at ϕ_L equals 0°. Thus although, as explained before, the scatterers
contributing power at a certain V_R are closer to the axis of symmetry of
the antenna when ϕ_L approaches 90°, their extent in azimuth and hence
their area on the earth surface is smaller. For relative velocities away
from V_R equals 0 m/s, the former effect dominates the latter because of
the narrow beamwidth of the antenna. But for V_R equals zero, by defini-
tion of V_R, the scatterers are boresighted with the antenna for both
ϕ_L equals 0 and 90 degrees. The latter effect only exists and results
in a somewhat lower clutter power for a ϕ_L of 90°.

Fig. 15 shows the SIR curve corresponding to the solid curve in
Fig. 13. Again for comparison, the SIR curve for ϕ_L = 0° is shown as a
dashed line. As expected, all the features of the clutter spectra are
evident on the SIR curves and for this reason only the SIR curves will be
analyzed for the rest of this report. Observe the larger MDV for ϕ_L
equals 90° [-62 m/s, 62 m/s] in Fig. 15. This example clearly illustrates
that the MDV depend not only on terrain but also on the geometry of the
satellite and the target. These effects will be described in detail in
Section 5.0.

Fig. 16 shows the superposition of the SIR curves for azimuth
angles of 0, 15, 30 and 90 degrees and grazing angle of 3°. This figure
illustrates that although the clutter power C_V is negligibly small for
V_R larger than 14 m/s when the antenna is aligned with the direction of
motion of the satellite (ϕ_L = 0°), this clear area fills in very rapidly
as ϕ_L increases until the spectrum becomes symmetrical when ϕ_L equals
85.86°. If ϕ_L increases even further, the radar antenna points progres-
sively in a direction opposite to the direction of motion of the satel-
lite. The clutter spectrum for any azimuth look angle equal to 180° -
ϕ_L is identical but reversed with respect to V_R equals zero, when com-
pared to the spectrum measured at ϕ_L. As an example, Fig. 17 shows the
clutter spectrum for γ = 3° but ϕ_1 equals 180° which is identical to the
case for which ϕ_L equals zero but with the velocity axis reversed. In
this case it would be easier to detect a target receding from the space-
craft at a speed in excess of approximately-14 m/s.

So far, examples for which the radar antenna was pointed at a low
grazing angle (γ_L = 3°) were investigated. It was shown that the clut-
ter spectra vary significantly when the azimuth look angle and also the
terrain changed. In the next sections, we will investigate the shape and
magnitude of the clutter for larger grazing angles. We will restrict our
attention to zero azimuth look angles since the effects observed for
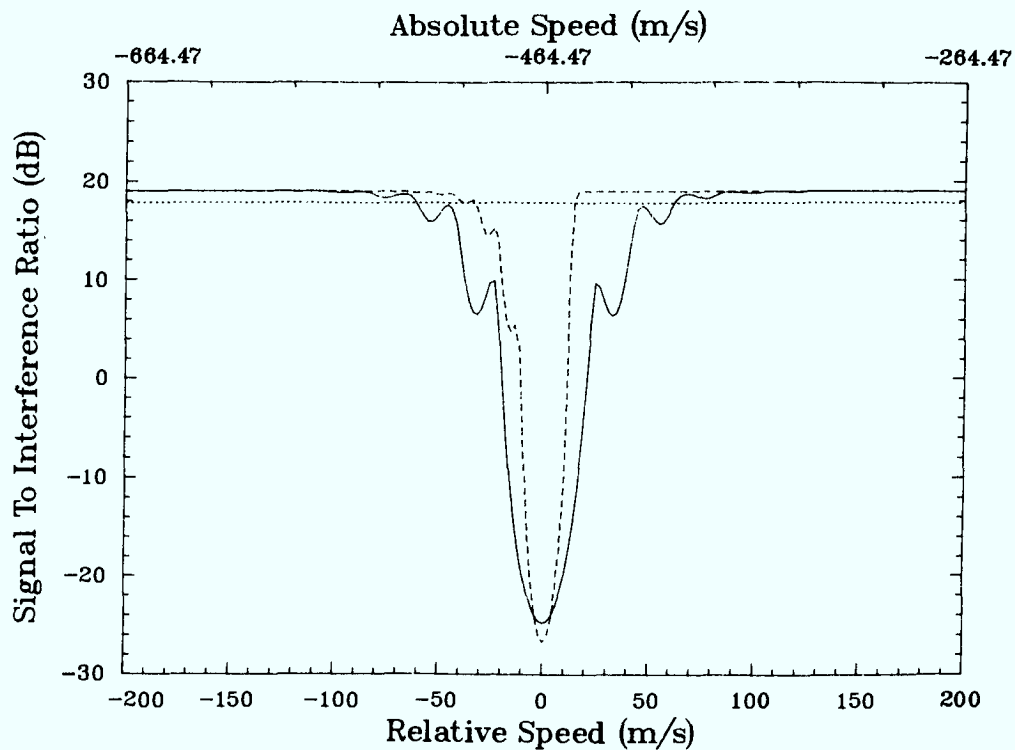larger ϕ_L are similar to those described in the previous section.

Figure 15 – Comparison of the SIR for $\phi_L=90°$ (continuous curve) and $\phi_L=0°$ (dashed curve) for a low grazing angle ($\gamma_r=3°$).
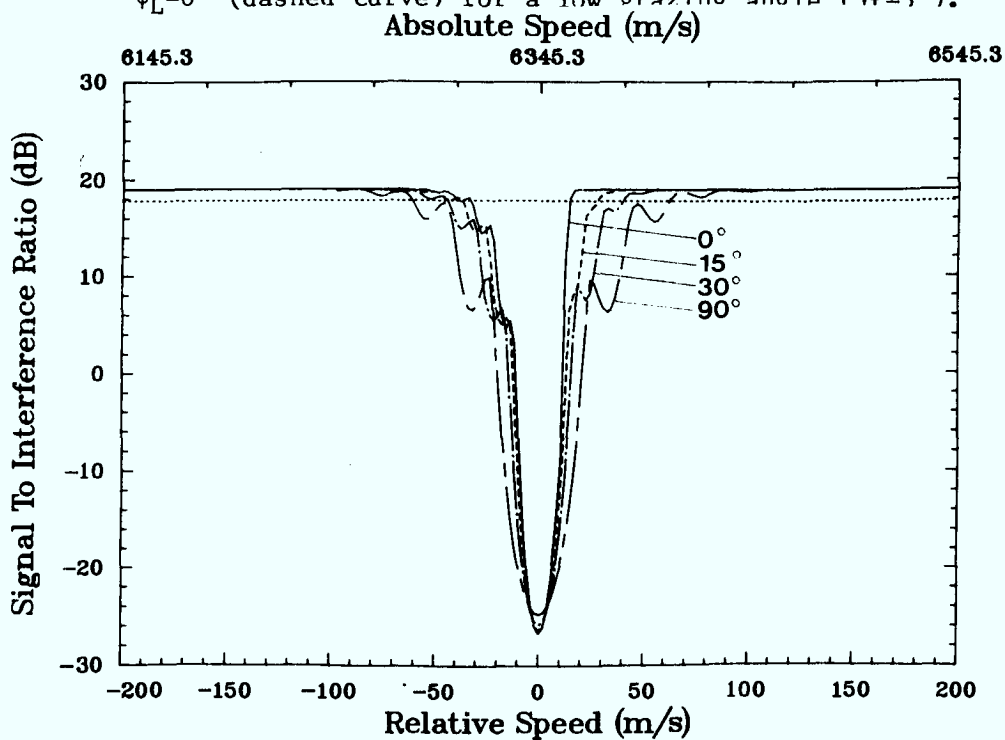

Figure 16 – Effect of the azimuth look angle on the SIR of the baseline system ($\gamma_L=3°$)

Absolute Speed (m/s)
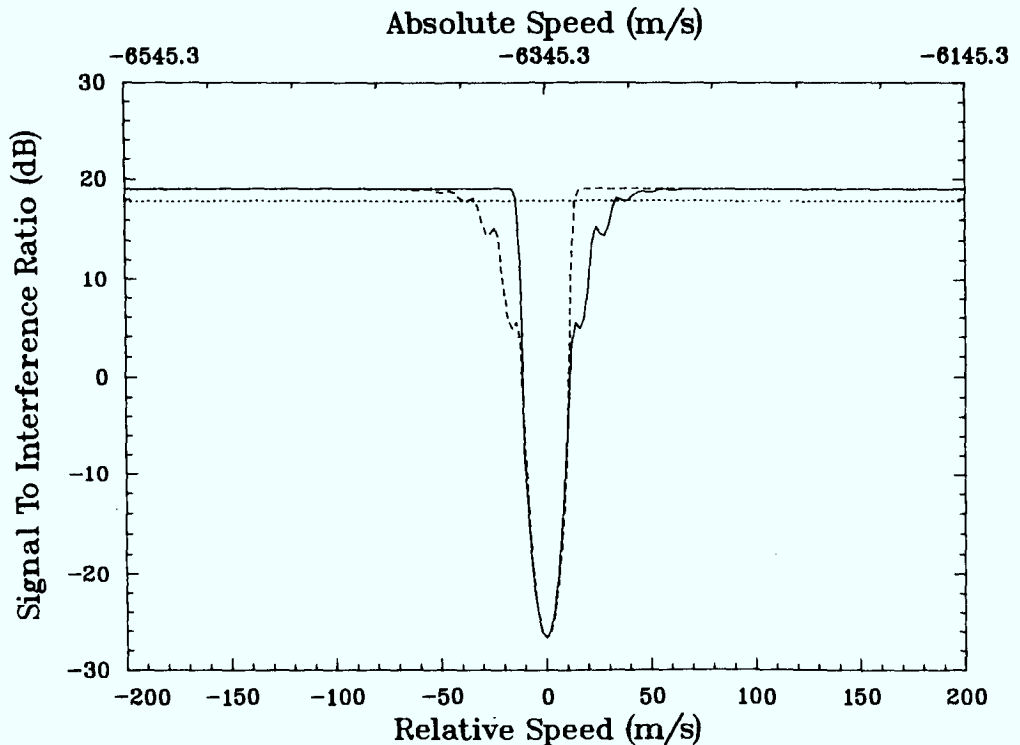

Figure 17 — Comparison of the SIR for $\phi_L=180°$ (continuous curve and $\phi_L=0°$ (dashed curve) at low grazing angle ($\gamma_L=3°$)

4.6   Effect of Grazing Angle

Fig. 18 shows the three dimensional clutter spectrum detected by an SBR when the antenna is pointed at a grazing angle of 30 degrees and is aligned with the direction of motion of the satellite ($\phi_L = 0°$). Fig. 19 is the isodop curve for this geometry.

The maximum clutter power occurs at $V_R = 0$ m/s ($V_o = 5502.7$ m/s), but there is no velocity at which the clutter power C_V is very small within our 400 m/s window as was the case when $\gamma_L = 3°$. The spectrum extends from -6373.19 m/s to 6373.19 m/s and because V_o is much smaller than these maximum speeds, no abrupt termination of the spectrum within a $\pm$ 200 m/s window is observed. Thus in the present situation any target travelling within ±200 m/s with respect to the satellite will have to compete with extensive clutter for detection.

The narrow extent of the clutter spectrum (Fig. 18) along the range line axis indicates that for most radial velocities, only one range line contributes significant power to the clutter spectrum. This is caused by the combined effect of the increased spacing between adjacent range lines at higher grazing angles (as seen in Fig. 2) and the smaller size of the foot print of the antenna.
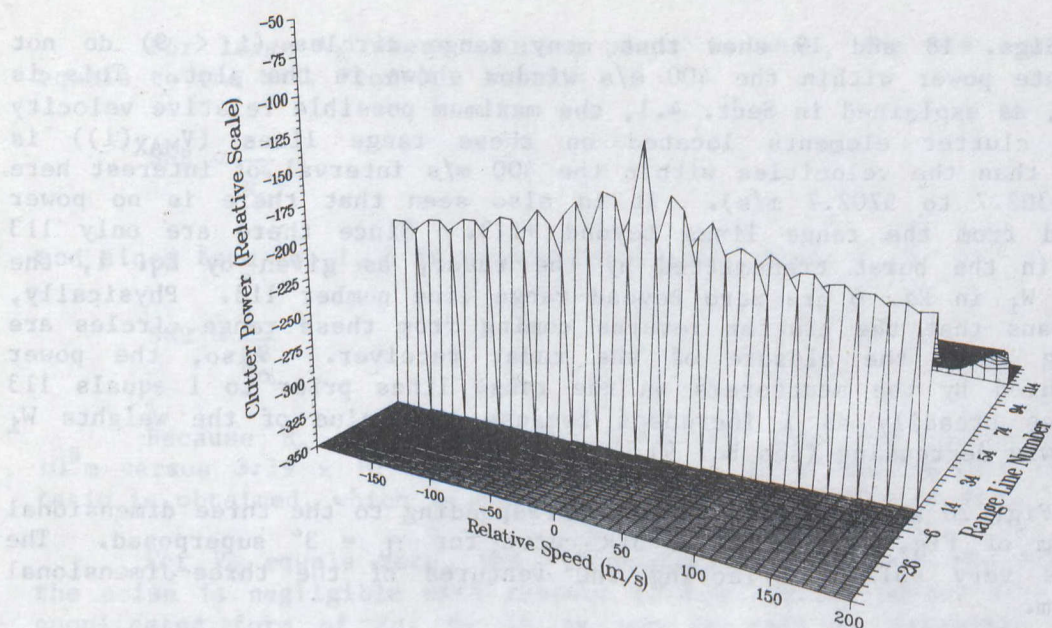
Figure 18 – Three-dimensional clutter spectrum for the baseline
system at 30° grazing angle ($\phi_L=0°$)

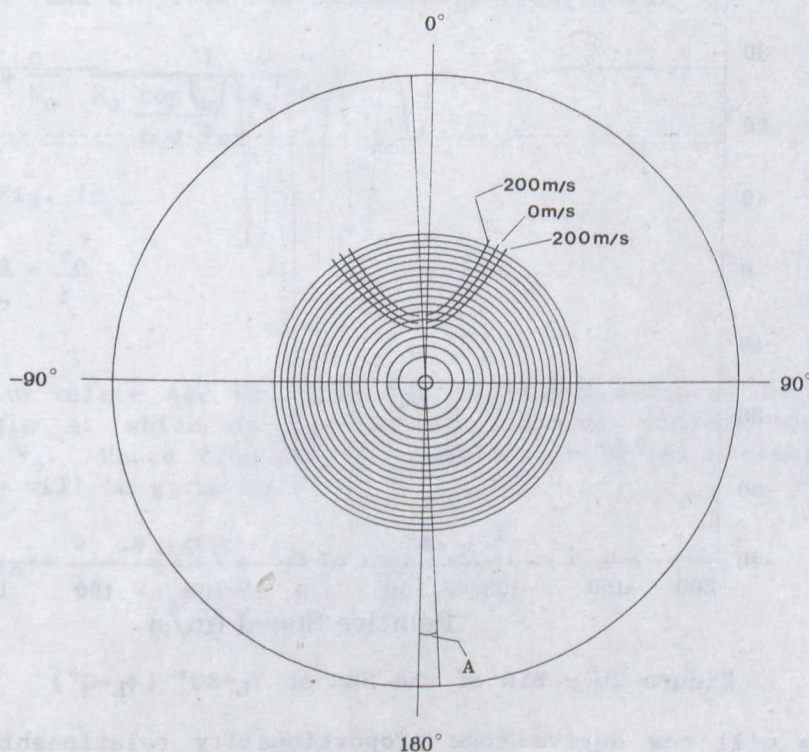Figure 19 – Isodops for the system at a grazing angle of 30° ($\phi_L=0°$)

Figs. 18 and 19 show that many range circles (i < 9) do not contribute power within the 400 m/s window shown in the plot. This is because, as explained in Sect. 4.1, the maximum possible relative velocity of the clutter elements located on these range lines ($V_{MAX}(i)$) is smaller than the velocities within the 400 m/s interval of interest here (from 5302.7 to 5702.7 m/s). It is also seen that there is no power returned from the range lines beyond +113. Since there are only 113 pulses in the burst transmitted by the radar, as given by Eq. 1, the weights W_i in Eq. 6 are zero beyond range line number 113. Physically, this means that the clutter returns coming from these range circles are arriving after the closure of the radar receiver. Also, the power contributed by the scatterers on the range lines prior to i equals 113 decreases steadily as i increases because the value of the weights W_i are slowly decreasing (see Eq. 9).

Fig. 20 shows the SIR curve corresponding to the three dimensional spectrum of Fig. 18, with the SIR curve for $\gamma_L = 3°$ superposed. The plot is very spiky, reflecting the features of the three-dimensional spectrum.

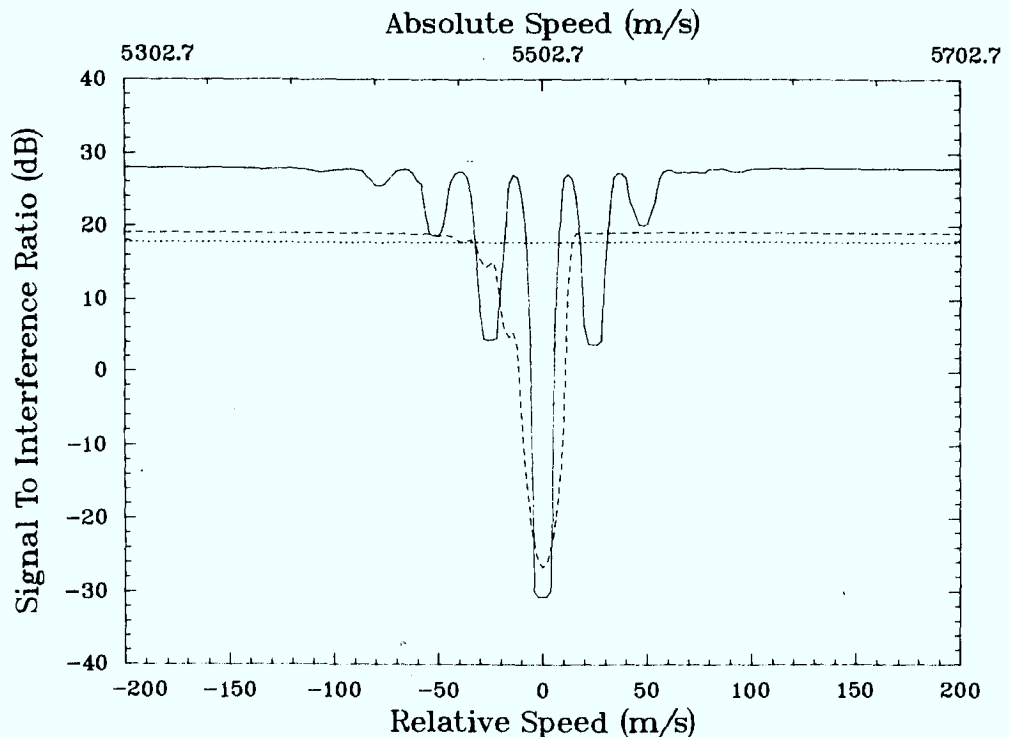Figure 20 - SIR of the SBR at $\gamma_L = 30°$ ($\phi_L = 0°$)

We will now derive some proportionality relationships to explain the variations in the values of SIR when the system is noise-limited (SIR≈SNR) and clutter-limited (SIR≈SCR).

For large V_R where clutter power is weak, the SIR approximately equals to the SNR. From Eq. 3 and 4

$$SNR \; \alpha \; \frac{n}{R_O^4} \tag{29}$$

and since from Eq. 1, n is proportional to R_O then:

$$SNR \; \alpha \; \frac{1}{R_O^3} \tag{30}$$

Because R_O is smaller for $\gamma_L = 30°$ than for $\gamma_L = 3°$ (1.70 x 10^6 m versus 3.39 x 10^6 m), approximately 8 dB of improvement in the SNR ratio is obtained, which is consistent with the results of Fig. 20.

For V_R equals zero, the SIR approximately equals the SCR because the noise is negligible with respect to the clutter power. With the more complicated form of Eq. 6, it is not as easy to establish a simple relationship between the SCR ratio and the grazing angle. But for large grazing angles the range lines become further apart and the clutter power at $V_R=0$ arises mainly from the clutter elements located on the main range line. The SCR can then be related to γ_O as follows. For i = 0, Eq. 4, 6, 20 and 27 yield the approximate relationship:

$$SCR \; \alpha \; \frac{n}{W_O} \; \frac{1}{R_O \; \dfrac{\cos \theta_O}{\cos \gamma_O} \; \Delta \phi_T \; \sigma(\gamma_O)} \tag{31}$$

where from Fig. 1c

$$\frac{\cos \theta_O}{\cos \gamma_O} = \frac{r_e}{r} \tag{32}$$

We can relate $\Delta \phi_T$ to ΔV in the following manner. Let ϕ_O be the azimuth angle at which is located the clutter element whose radial velocity is V_O. Hence from Eq. 10, expanded in Taylor series, the upper bound of $\Delta \phi_T$ will be given by

$$\phi_{UPPER} = \frac{\pi}{2} - \frac{V_O + \Delta V/2}{V_{MAX}(i=0)} - \frac{1}{6} \frac{(V_O + \Delta V/2)^3}{V_{MAX}^3(i=0)} - \cdots \quad -A \tag{33}$$

Note that Eq. 33 only applies for $V_0 + \Delta V/2 \ll V_{max}$

Subtracting the lower bound of the azimuth interval (obtained by replacing $\Delta V/2$ by $-\Delta V/2$ in Eq. 33) from its upper bound, we obtain

$$\Delta \phi_T = \frac{\Delta V}{V_{MAX}(i=0)} - \frac{1}{6} \frac{(V_0 - \Delta V/2)^3}{V_{MAX}^3(i=0)} + \frac{1}{6} \frac{(V_0 + \Delta V/2)^3}{V_{MAX}^3(i=0)} - \ldots + \ldots \quad [34]$$

Keeping only the terms linear in ΔV, we will obtain

$$\Delta \phi_T \simeq \frac{\Delta V}{V_{MAX}(i=0)} + \frac{V_0^2 \ \times \ \Delta V/2}{V_{MAX}^3(i=0)} \quad [35]$$

For the case of interest here, ϕ_L equals $0°$ and $V_0 \simeq V_{MAX}$. Hence

$$\Delta \phi_T \ \alpha \ \frac{\Delta V}{V_{MAX}(i=0)} \quad [36]$$

finally making use of the fact that

$$V_{MAX}(i=0) \ \alpha \ \ V_{MAX} \cos \gamma_0 \quad [37]$$

we obtain

$$\Delta \phi_T \ \ \alpha \ \ \frac{\Delta V}{\cos \gamma_0} \quad [38]$$

From Eq. 19 it can be written that

$$\Delta V \ \alpha \ 1/T_B \quad [39]$$

But since T_B is proportional to the total number of pulses in the burst, itself related to R_0 according to Eq. 1, we have

$$\Delta V \ \alpha \ \frac{1}{R_0} \quad [40]$$

Finally, for i equals 0, W_0 equals n and by substituting Eqs. 32, 38 and 40 into Eq. 31:

$$SCR \ \alpha \ \frac{\cos \ \gamma_0}{\sigma(\gamma_0)} \hspace{4cm} [41]$$

Unfortunately, this relation cannot be used to compare the SCR for γ_L = 30° to the one for γ_L equals 3°. Although it applies for γ_L = 30°, it is not accurate at low grazing angles since the clutter power at V_R = 0 m/s does not only arise from scatterers located at i = 0. If we were to use Eq. 41 we would find that SCR $_{30°}$ should be 14 dB smaller than SCR$_{3°}$. (cos 30°/cos3° = 0.6 dB, $\sigma_0(3°)/\sigma(30°)$ = 13 dB.). This is not what is observed from Fig. 20 where SCR$_{30°}$ is smaller than SCR$_{3°}$ by only about 4 dB. This is caused by the large number of range lines within the main lobe of the antenna when γ_L equals 3° whereas there is only one when γ_L equals 30°. Eq. 41 will be found in good agreement with the results obtained for the next cases.

When the radar antenna is pointed at a still steeper grazing angle, (γ_L = 60°) the three dimensional spectrum of Fig. 21 results. For clarity, the viewpoint used to plot Fig. 21 is located opposite with respect to the range line axis to that chosen in the previous examples.

Compared to the case for γ_L = 30°, R_0 decreases for γ_L = 60° (R_0 = 1.13 x 10^6m), the footprint of the antenna is smaller and the range circles are even further apart. Fig. 21 clearly shows that only two sidelobes in the clutter spectrum are significant in addition to the main-lobe clutter. A detailed analysis not given here shows that they result from the first sidelobes of the antenna intersecting the range circles i equal + 1 and -1. It should be noted however that the clutter power between the peaks of Fig. 21 although small is not zero.

Fig. 22 compares the SIR curves for γ_L = 60° and γ_L = 30°. In areas of low clutter power, an improvement of approximately 5 dB in the SNR results from the smaller range when γ_L equals 60°, as per Eq. 30 ($(R_{30°}/R_{60°})^3$ equals 5.3 dB). On the other hand, when V_R equals 0 m/s the SCR is approximately 20 dB poorer. Since there is only one range line within the main lobe of the antenna for both γ_L equals 60° and 30°, Eq. 41 applies and the decrease in the SCR correlates well with the value observed in Fig. 22 (cos60°/cos30° = -2.4 dB and $\sigma_0(60°)/\sigma_0(30°)$ = 18 dB).

Finally, it is worth pointing out that the width of the main lobe of the SIR curve for γ_0 equals 60° is somewhat larger than for γ_L equals 30°. This is caused by the larger ΔV arising from a shorter burst duration as R_0 decreases (see Eq. 19).

When the radar antenna is pointed in a direction such that it is almost normal to the surface of the earth (γ_L=85°), the three dimensional clutter spectrum of Fig. 23 and the corresponding SIR curve of Fig. 24 result (th dashed curve is for γ_L=60°. There is only one mainlobe in the clutter spectrum within the 400 m/s window of interest since the foot-
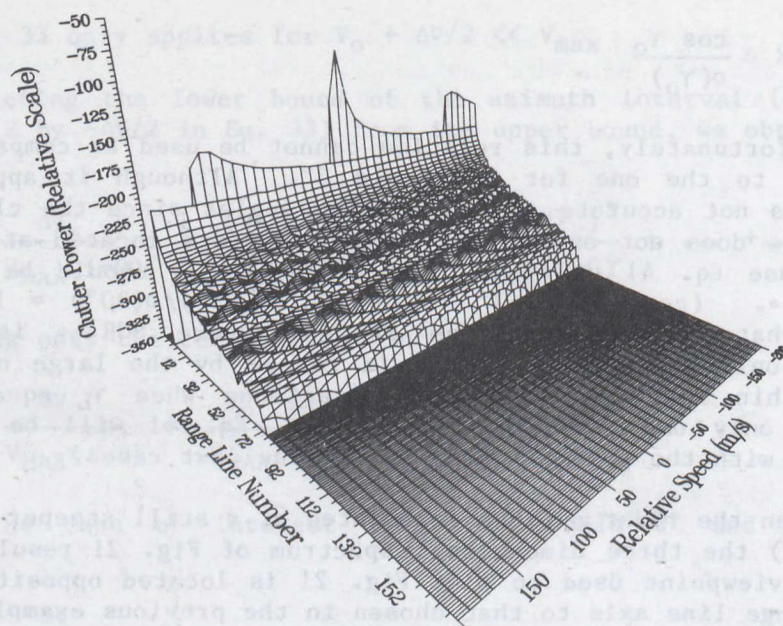
Figure 21 – Three-dimensional clutter specrum for the SBR
when γ_L equals 60° ($\phi_L=0°$)
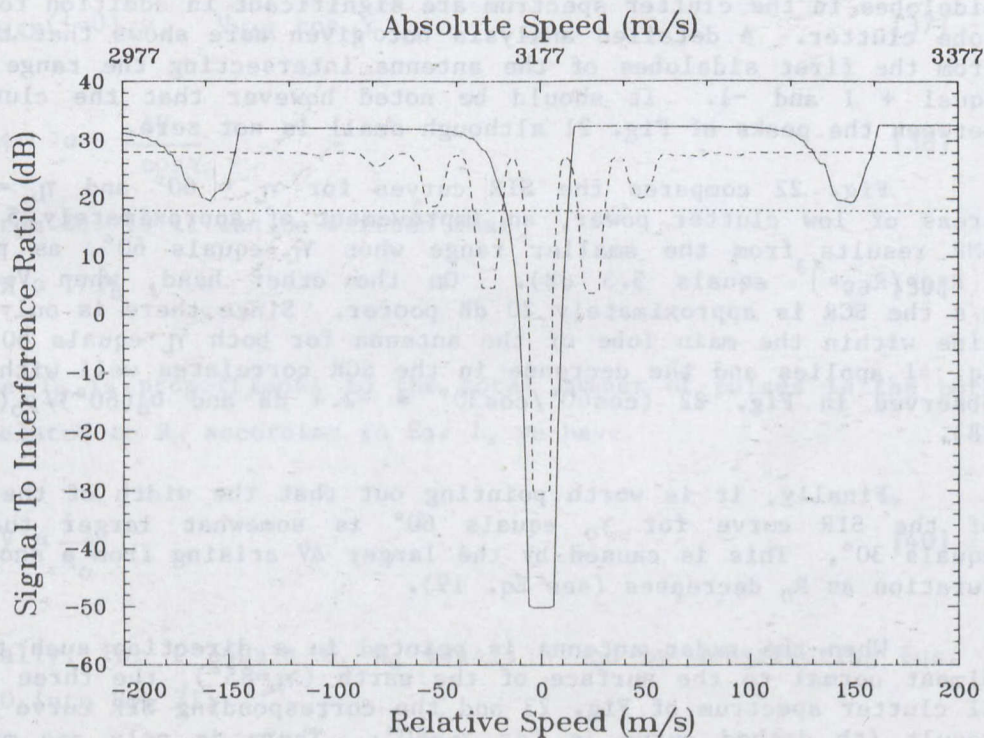

Figure 22 – SIR for the baseline system at a grazing angle of
60° ($\phi_L=0°$)
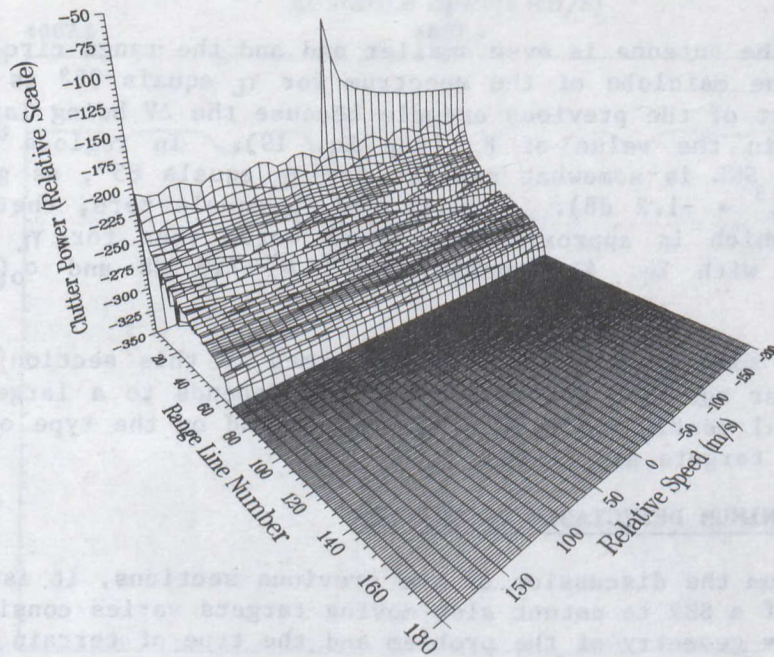
Figure 23 – Three-dimensional clutter spectrum for the baseline
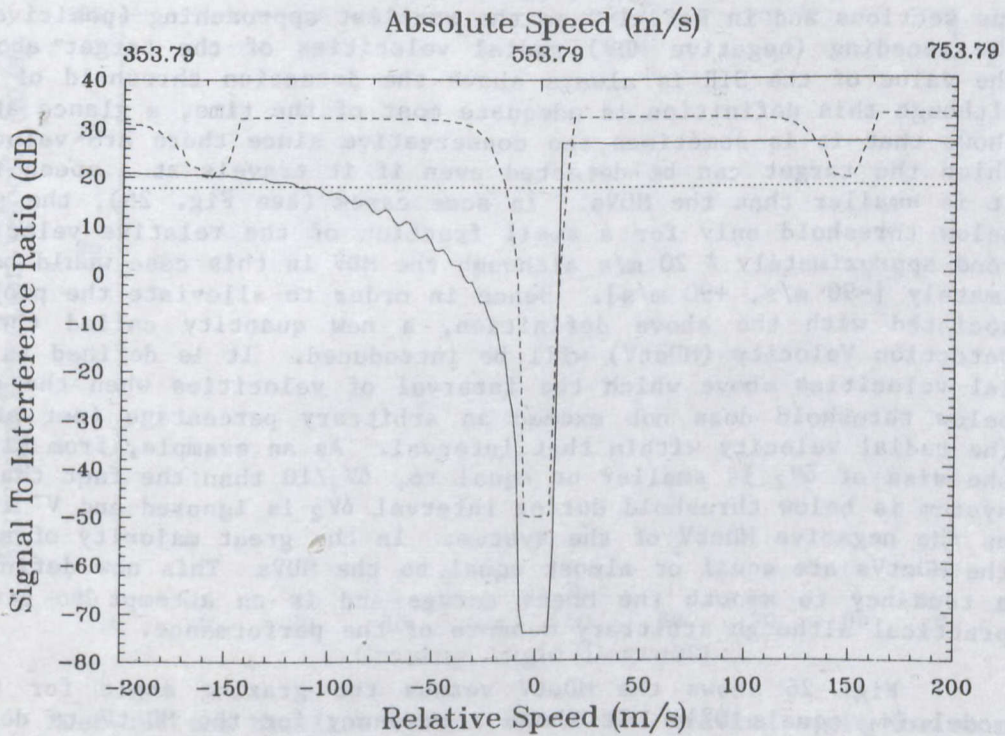system for γ_L equals 85° ($\phi_L=0°$)

Fig. 24 – SIR for the baseline system at a grazing angle of 85° ($\phi_L=0°$)

print of the antenna is even smaller and and the range circles are further apart. The mainlobe of the spectrum for γ_L equals 85° is wider than its counterpart of the previous example because the ΔV being larger due to the decrease in the value of R_o (see Eq. 19). In regions of low clutter power the SNR is somewhat smaller for γ_L equals 85°, as given by Eq. 30 $\left(\left(R_{85}/R_{60} \right)^3 = -1.2 \text{ dB} \right)$. Finally for V_R equals zero, the SIR reduces to the SCR which is approximately 24 dB worse than for γ_L equals 60°, in agreement with Eq. 41 $(\cos 85°/\cos 60° = -7.6 \text{ dB}$ and $\sigma_o(85°)/\sigma_o(60°) = 16 \text{ dB})$.

In summary, the analysis performed in this section has shown that the clutter spectrum detected by an SBR depends to a large extent on the geometrical configuration of the problem and on the type of terrain above which the targets are flying.

5. MINIMUM DETECTABLE VELOCITIES

From the discussion of the previous sections, it is clear that the ability of a SBR to detect slow moving targets varies considerably according to the geometry of the problem and the type of terrain above which the targets are flying. In this section the minimum velocities of the targets which can be detected by a real aperture space based, pulse doppler radar will be analyzed.

The minimum detectable velocities (MDV) were defined in the previous sections and in Ref. 1-2 as the smallest approaching (positive MDV) or the receding (negative MDV) radial velocities of the target above which the value of the SIR is always above the detection threshold of the SBR. Although this definition is adequate most of the time, a glance at Fig. 20 shows that it is sometimes too conservative since there are velocities at which the target can be detected even if it travels at a speed for which it is smaller than the MDVs. In some cases (see Fig. 25), the system is below threshold only for a small fraction of the relative velocities beyond approximately $\pm$ 20 m/s although the MDV in this case would be approximately [-90 m/s, +90 m/s]. Hence in order to alleviate the problems associated with the above definition, a new quantity called the Minimum Detection Velocity (MDetV) will be introduced. It is defined as the radial velocities above which the interval of velocities when the system is below threshold does not exceed an arbitrary percentage (set at 10%) of the radial velocity within that interval. As an example, from Fig. 25, if the size of δV_2 is smaller or equal to, $\delta V_1/10$ than the fact that the SBR system is below threshold during interval δV_2 is ignored and V^- is defined as the negative MDetV of the system. In the great majority of situations the MDetVs are equal or almost equal to the MDVs This new definition has a tendancy to smooth the MDetV curves and is an attempt to give a more practical although arbitrary measure of the performance.

Fig. 26 shows the MDetV versus the grazing angle for the ocean model (ϕ_L equals 0°). It shows a tendancy for the MDetV to decrease as γ_L increases which reflects the fact that the width of the SIR curves is decreasing, as was observed in the previous sections. The undulations in the MDetV curves are not very significant. They arise when the side-
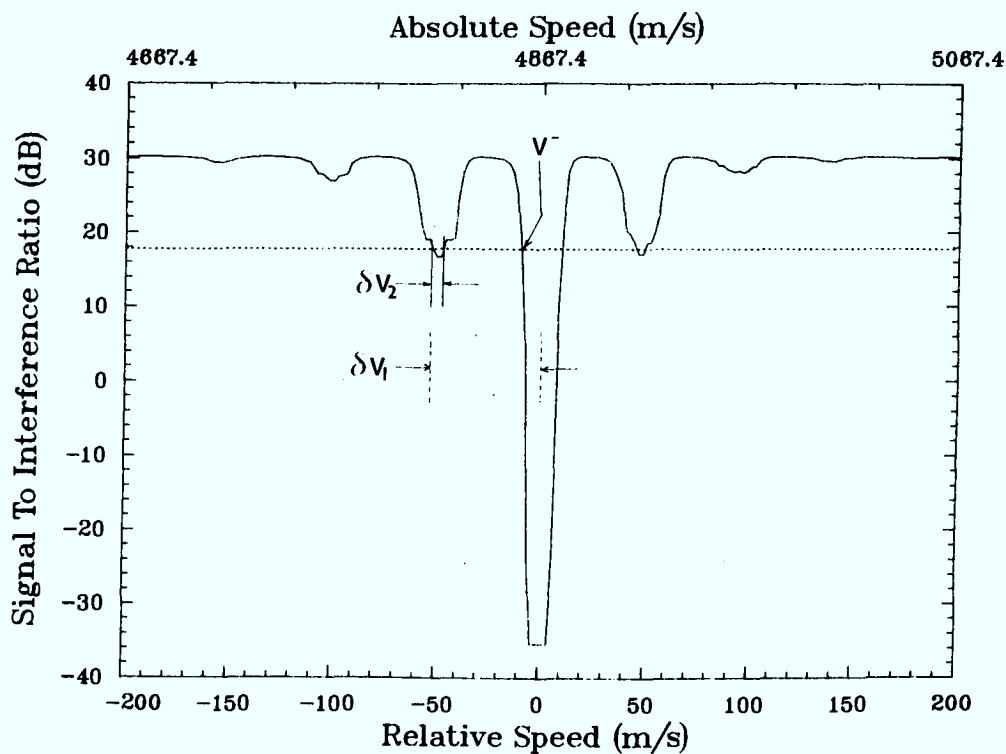
Fig. 25 - SIR for the baseline system at a grazing angle of 50° (ϕ_L=0°)
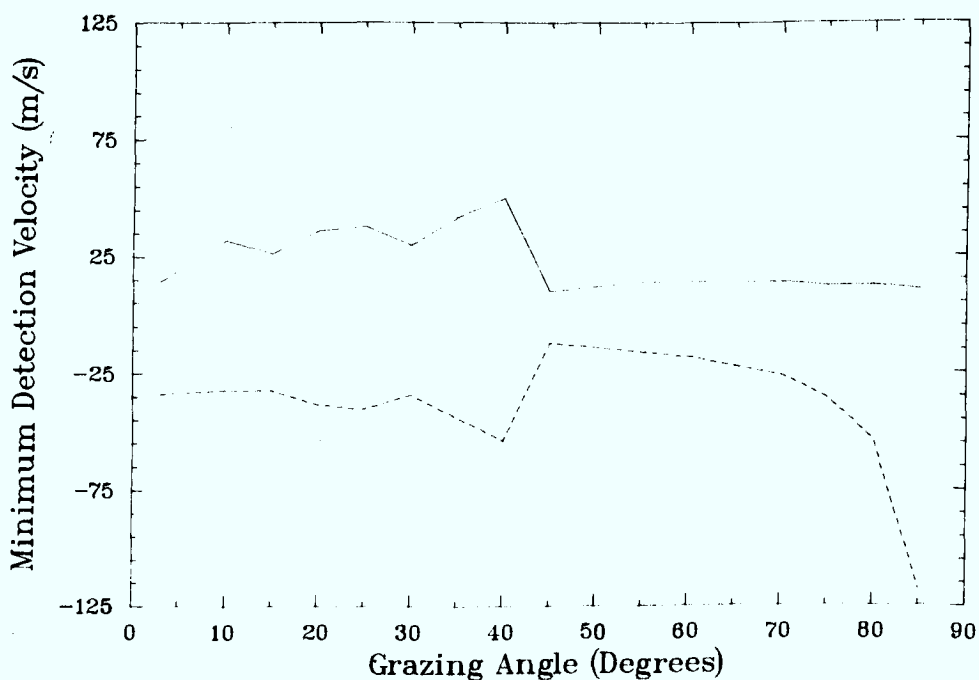

Fig. 26 - MDetV of the baseline system versus the grazing angle for an ocean background (ϕ_L=0°). The solid line is for the positive MDetV whereas the dashed line is for the negative MDetV.

lobes of the antenna are coincident with the location of the ambiguous range circles on the surface of the earth. This causes the sidelobes in the corresponding SIR curves to be more or less important, which produces in turn some non-uniformity in the MDetV as the geometry changes. It should also be observed that the low value of the positive MDetV near grazing incidence is caused by the clutter free region at low grazing angle. The sharp drop in the MDetV for γ_L equals $50°$ arises when the sidelobe of the SIR curve are no longer deep enough to determine the MDetV (i.e. $\delta V_2 < \delta V_1/10$ in Fig. 25). Finally, the increase of the MDetV near normal incidence is caused by the broadening of the SIR curve for large grazing angles (see Fig. 24).

It is worth mentioning that the decrease of the MDetV for larger grazing angle does not necessarily mean that an SBR system would operate more successfully at a higher grazing angle. When a target is flying on a course which is roughly parallel to the surface of the earth its radial velocity is likely to be a smaller fraction of its air speed as the grazing angle increases. Thus although the MDetV are getting smaller, so does the likely radial velocity of the target and hence the harder it becomes to detect. As a result of this and also because some expressions in our simulation are inaccurate beyond $\gamma_L = 85°$, the MDVs were not computed for $\gamma_L > 85°$. However, it is expected that until the radar antenna is pointed within a beamwidth of normal incidence the MDVs will grow larger as γ_L increases beyond $85°$ since the extent of one range resolution cell on the surface of the earth becomes a large fraction of the footprint of the radar. As γ_L approaches $90°$, the SIR versus V_R curve becomes symmetric and the MDVs are approximately $\pm$ 120 m/s.

Fig. 27 shows the MDetV as a function of γ_L when the terrain background is ice, along with that for the ocean. It shows that at low grazing angles, the MDetVs for the ice are approximately twice as large as those for the ocean. However, as the grazing angle becomes larger the MDetVs become nearly identical since as shown in Fig. 3, their σ_o become almost equal. A plot of the MDetV for the snow model is not shown since it is intermediary between the ocean and the ice and it exhibits the same general features. These curves show that the terrain above which potential targets are flying has a very significant effect on the performance of the SBR when the antenna is pointed at a small grazing angle. As mentioned above, this is the situation of greater interest in practice since the radial velocity of the targets is likely to be greater for low grazing angle than when the antenna is almost normal to the surface of the earth.

Fig. 28 shows the effect of the azimuth-look angle on the MDetV for an ocean and an ice background at low grazing angle. In both cases, the MDetV increase as ϕ_L increases, as described in Section 4.5. For small ϕ_L the positive MDetVs are significantly smaller than the negative ones because of the clutter free area for the positive radial velocities of the system (see Fig. 16). As discussed in Section 4.5 the MDetV is symmetrical with respect to $\phi_L = 90° -A$. Hence the MDetV for $\phi_L > 90°$ can be found from Fig. 28.

The effect of terrain type on the MDetV as a function of the azimuth look angle is very pronounced. As seen from Fig. 28, the MDetV is more than twice as large for the ice as compared to the ocean case over most of the interval from $\phi_L = 0°$ to $90°$.

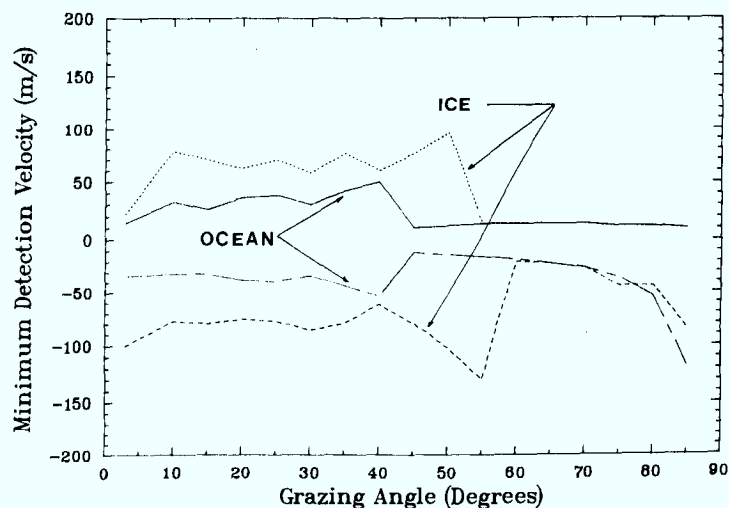

Figure 27 – Comparison of the MDetV versus grazing angle for
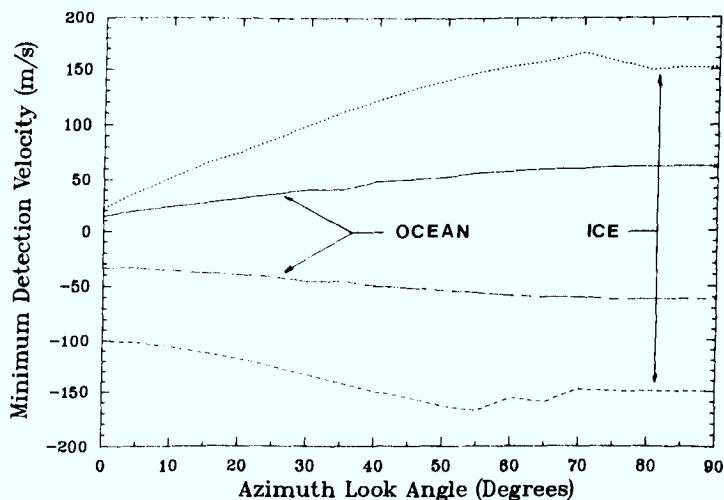ice and snow backgrounds. (ϕ_L=0°)

Figure 28 – Comparison of the MDetV versus the azimuth-look angle
for ice and snow backgrounds. (γ_L=3°)

6. __CONCLUSION__

A detailed analysis of the features of the clutter spectrum received by an SBR under various geometrical configurations and for different types of clutter background was presented in this report. The ability of an SBR surveillance systems to detect slow moving targets was also investigated through the analysis of the minimum detection velocities of the baseline radar under various conditions.

The main findings of this report can be summarized as follows:

a) Clutter spectra depend to a large extent on the geometry of encounter between the SBR and the target. Generally speaking the spectra become narrower (smaller MDV) as the grazing angle increases except near normal incidence at which point they become broader (larger MDV). Also the peak of the spectrum becomes larger for large grazing angles. As the radar is pointed progressively away from the direction of motion of the satellite, the spectra broaden.

b) The minimum velocity of targets which can be detected by an SBR varies with the type of terrain over which it is flying, especially when the antenna pattern exhibits very large sidelobes. At low grazing angles, the interference caused by clutter is progressively lower for ice, snow and ocean. At larger grazing angles (above approximately 60°), the clutter power does not depend very much on terrain since, for the models investigated, the clutter cross-sections are almost equal.

The illumination function of the radar antenna was assumed to be uniform for the calculations done in this work. Since it is well known that weighting the illumination function of an antenna alters significantly its radiation pattern, it is interesting to investigate this effect on the results presented. Some of the calculations done in the previous sections were redone in the appendix for the case of a 40 dB Taylor weighting of the antenna pattern. The results obtained show a significant reduction of the clutter power coming into the receiver through the sidelobes of the antenna. Also, it is found that the MDetVs of the system become much less sensitive to the terrain type. Although the results presented in the Appendix are fragmentary, they show very clearly that the performance of the SBR system can be improved by properly weighting the illumination function of the radar antenna, at the expense of an increase in system complexity.

The results obtained here will be useful in designing SBR constellations for surveillance purposes. From this report, it is seen that low and ultra low sidelobe antennas are very desirable both to reduce the minimum velocity of the targets which can be detected and to obtain performances which do not depend significantly on the type of clutter background

For best performances, the coverage of the individual radars within the constellation could be confined within a small angle around the direction of motion of the satellite. However, the magnitude of that angle will have to be traded-off against the total number of radars required in the constellation.

Although rather small minimum detection velocities have been reported here, the use of other clutter cancellation techniques would enhance further the performances of SBR surveillance systems. The results presented here will also be useful when those studies are undertaken since they provide a detailed analysis of the magnitude and shape of the spectra detected by real aperture systems.

7. REFERENCES

1. Bird, J.S. and A.W. Bridgewater, "Performance of Space-based Radar in the Presence of Earth Clutter", IEE Proceedings, Vol. 131, Pt. F, No. 5, August 1984.

2. Rook, B.J., J.S. Bird and A.W. Bridgewater, "Detection of Near-Earth Targets by Space-based Radar: Development and Use of Computer Simulations", CRC Report No. 1389, July 1985.

3. Meyer, D.P. and H.A. Mayer, "Radar Target Detection - Handbook of theory and Practice", Academic Press, 1973.

4. Russel, R.A., T.G. Campbell and R.E. Freeland, "NASA Technology for Large Space Antennas", 31st Intl. Astronautical Congress of the Intl. Astronautical Federation, Tokyo, 21-28 Sept. 1980.

5. Skolnik, M.I., "Radar Handbook", McGraw-Hill, 1970.

6. Stiles, W.H., F.T. Ulaby, A.K. Fung and A. Aslam, "Radar Spectral Observations of Snow", IEEE Intl. Geosci. and Rem. Sens. Symp. (IGARSS'81) Digest, Washington, D.C., 1981.

7. Onstott, R.G., R.K. Moore and W.F. Weeks, "Surface-Based Scatterometer Results of Arctic Sea Ice", IEEE Trans. on Geosci. Electr, Vol. GE-17, No. 3, July 1979.

8. Mrstik, A.V., and A.C. Ludwig, "Multi-Frequency Reflector Antenna Study", General Research Corporation Report No. GRC-CR-1-1015 - Vol. 2, June 1981.

APPENDIX
TAYLOR WEIGHTING OF THE ANTENNA PATTERN

By weighting the illumination function of the radar antenna, it is possible to reduce the sidelobes of its radiation pattern. This is desirable since it will decrease the amount of clutter power creeping into the receiver through the sidelobes of the gain pattern of the antenna. It should be noted that this reduction in the amplitude of the sidelobes always results in a broadening of the mainlobe of the pattern which inevitably increases the mainlobe clutter. However the overall effect of weighting is beneficial in terms of reduced minimum detectable velocities.

There are many ways of weighting the illumination function of an antenna (Ref. 8). Some techniques attempt to minimize the ratio of the amplitude of the the close-in sidelobes with respect to mainlobe whereas others minimize the so-called integrated sidelobe ratio. A separate study would be required to investigate fully which of these approaches would be optimum for SBR operation. Since the intent of this Appendix is only to illustrate that we can improve the performance of an SBR by weighting its antenna pattern, a single example using 40 dB Taylor weighting for the antenna illumination function was used. Fig. Al compares the weighted to the unweighted pattern which was used in previous sections. As seen in the figure, the amplitude of the first sidelobe is 40 dB lower than the main lobe amplitude and the beamwidth of the weighted pattern is larger.
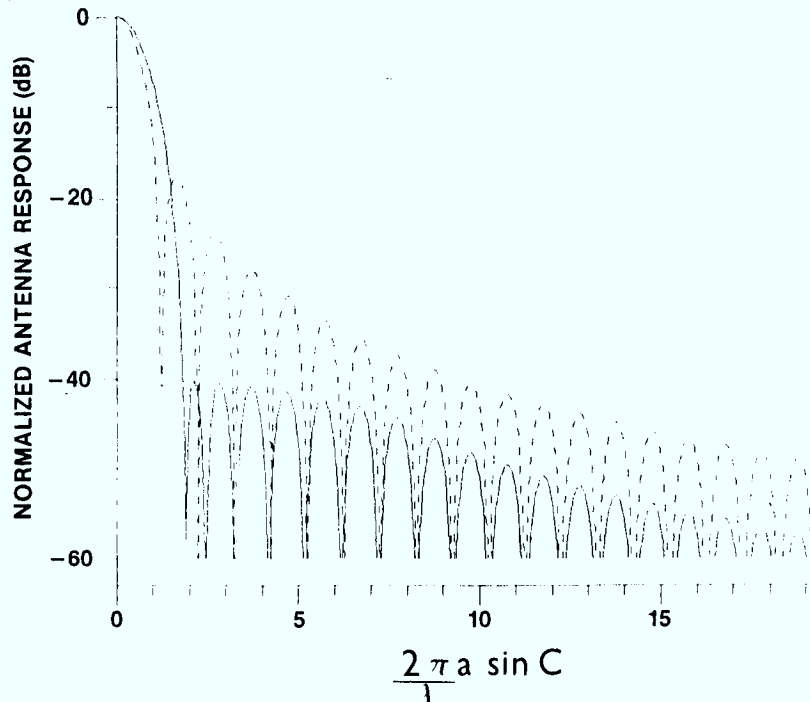

$$\frac{2 \pi a \sin C}{\lambda}$$

Figure Al – Comparison of the antenna patterns for a uniformly and a Taylor weighted aperture. The paramter a is the diameter of the antenna and C is the angle from the axis of symmetry of the antenna.

Because the effect of Taylor weighting is similar for all geometries and terrain studied so far, the discussion will be restricted to the geometry resulting in the broadest clutter spectrum. The antenna was pointed at a low grazing angle (γ_L equals 3°) and normal to the direction of motion of the satellite (ϕ_L equals 90°). Fig. A2 is the resulting three dimensional clutter spectrum (compare with Fig. 12) whereas Fig. A3 is the resulting SIR curve superposed on the one for the unweighted aperture. It is clear that the amount of clutter arising from clutter elements aligned with the sidelobes of the antenna has been reduced. However Fig. A3 shows that the mainlobe of the SIR curve is wider because of the widening of the mainlobe of the gain pattern, which also accounts for the slight increase in clutter power at small relative velocities. Despite this the MDV of the system is improved considerably, dropping to [−36 m/s, 36 m/s] from [−62 m/s, 62 m/s] for the unweighted case. All the other features of the spectrum of Fig. A2 and A3 are similar in nature to those of the unweighted spectra and will not be discussed further.

Fig. A4 shows the MDetV curves when Taylor weighting is applied to the antenna system (superposed on the MDetV curve without weighting for comparison). All the other parameters are the same as those in Fig. A3. It shows a decrease in the MDetV for all grazing angles but the decrease is not as large at higher grazing angles. Because of the smaller foot print of the radar and the increased spacing between the range lines at higher grazing angles most clutter power comes into the radar through the mainlobe of the antenna. In these cases, rejection of sidelobe clutter is not as important and the improvement of the MDetV is not as great.

Fig. A5 compares the MDetV vs γ_L curve for the ocean and the ice model. It shows that when the sidelobe level of the antenna pattern is reduced the MDetVs of the SBR becomes almost totally independent of the terrain. Fig. A6 shows the MDetV vs ϕ_L curves for the ocean and the ice model. The same conclusion holds that the performance of the SBR system became almost independent of terrain.

The example presented in this Appendix shows that by weighting the illumination function of the antenna, a significant reduction in the MDetVs of an SBR can be achieved and that the MDetVs can become much less dependent on the terrain type. This is achieved at the expense of some increased system complexity.

Finally, it is mentioned that if the weighting applied by the illumination function of the antenna is not as heavy as the one described in this section (i.e. larger sidelobes) the reduction in clutter power will not be as large. Refs. 8 and 9 indicate that 40 dB weighting has been achieved in practice and although it would certainly be difficult to implement on a large antenna such as the one used for this report, 40 dB Taylor weighting appears to be a reasonable achievement for which to aim.
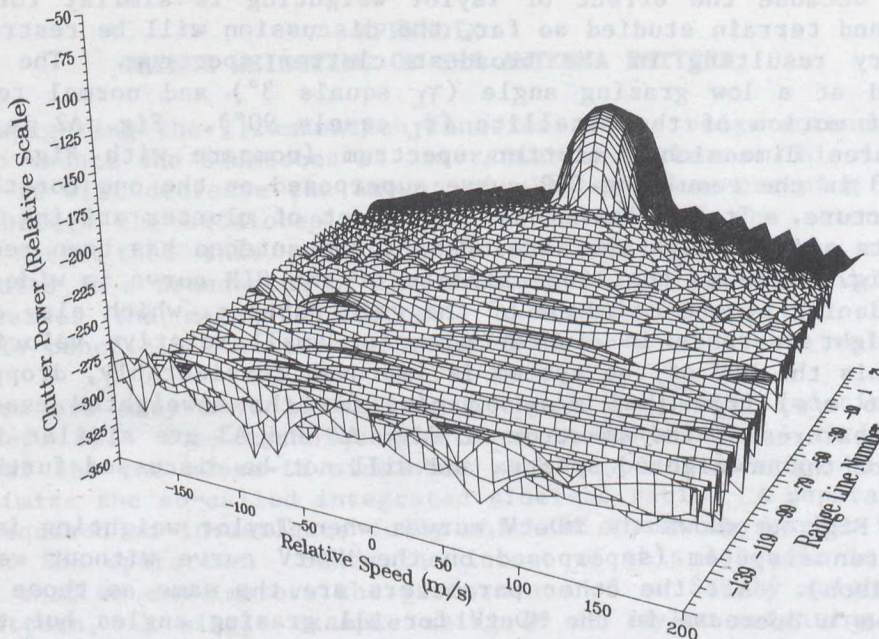
Figure A2 – Three-dimensional clutter spectrum for the base line system with a Taylor weighted aperture ($\gamma_L=30°$, $\phi_L=0°$)
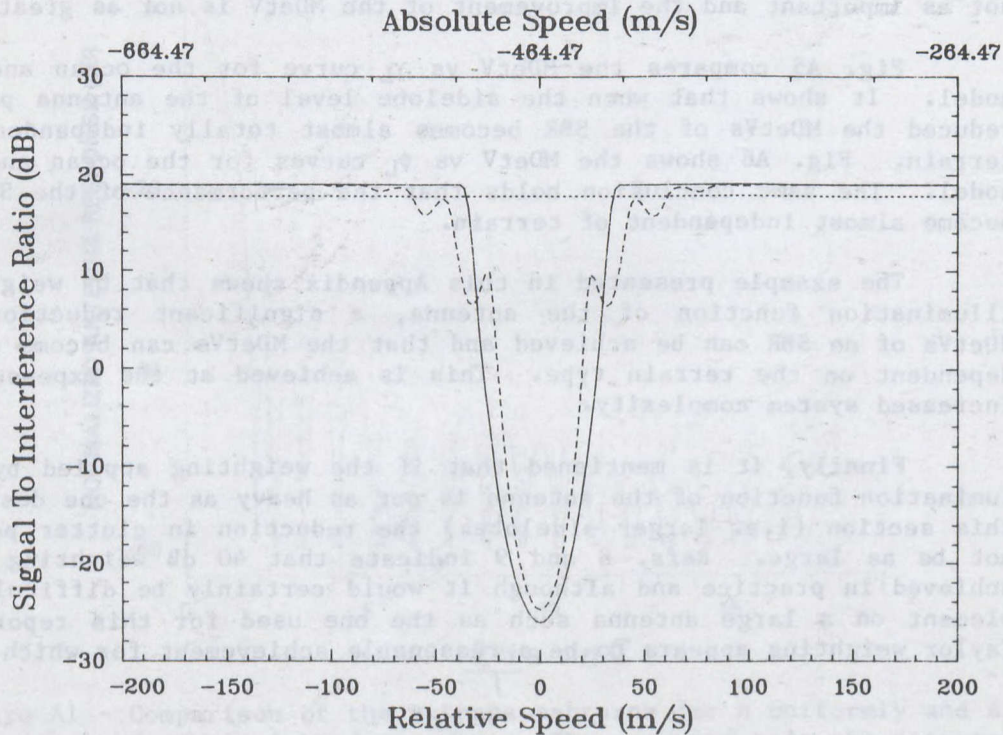

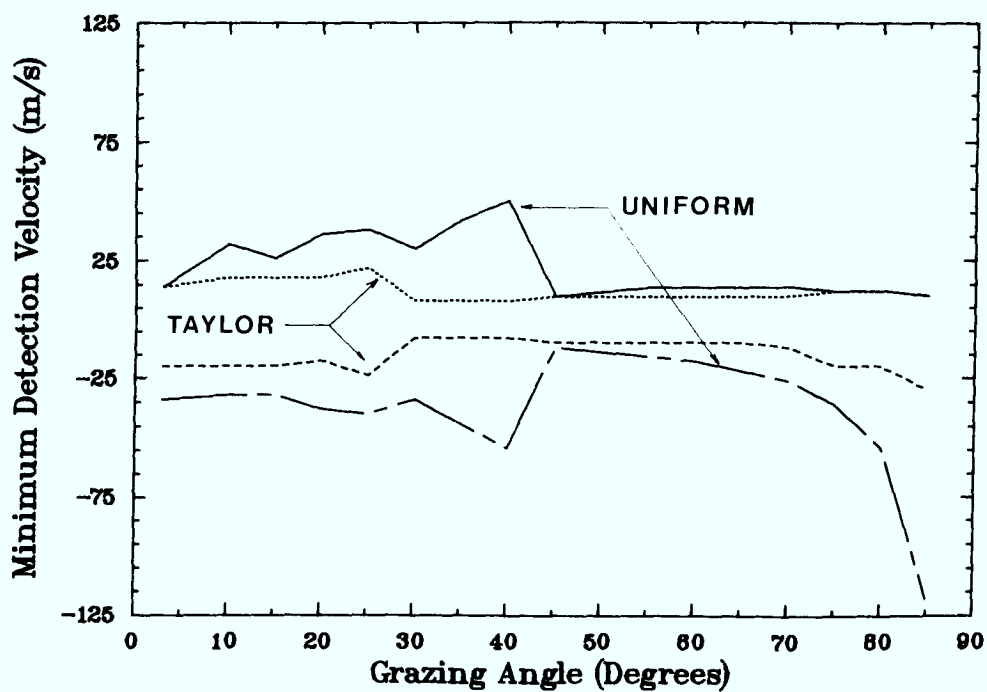Figure A3 – Clutter spectrum corresponding to the cae of Figure A2

Figure A4 – Comparison of the MDetV versus the grazing angle for a weighted and an unweighted aperture (ocean background $\phi_L=0°$)

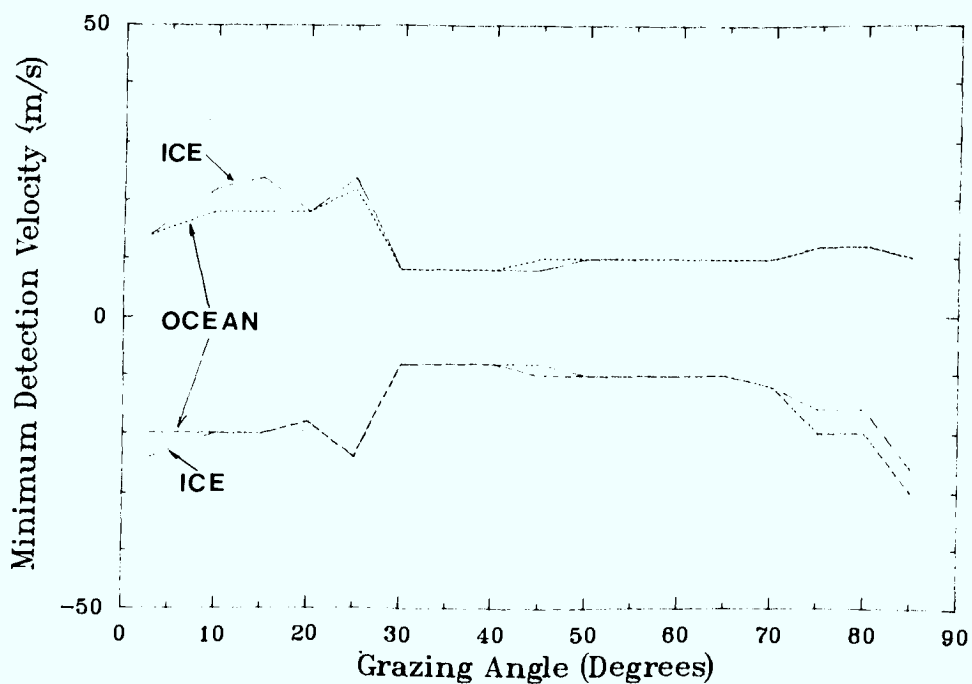Figure A5 – Comparison of the MDetV versus the grazing angle for ice and ocean background using weighted apertures ($\phi_L=0°$).

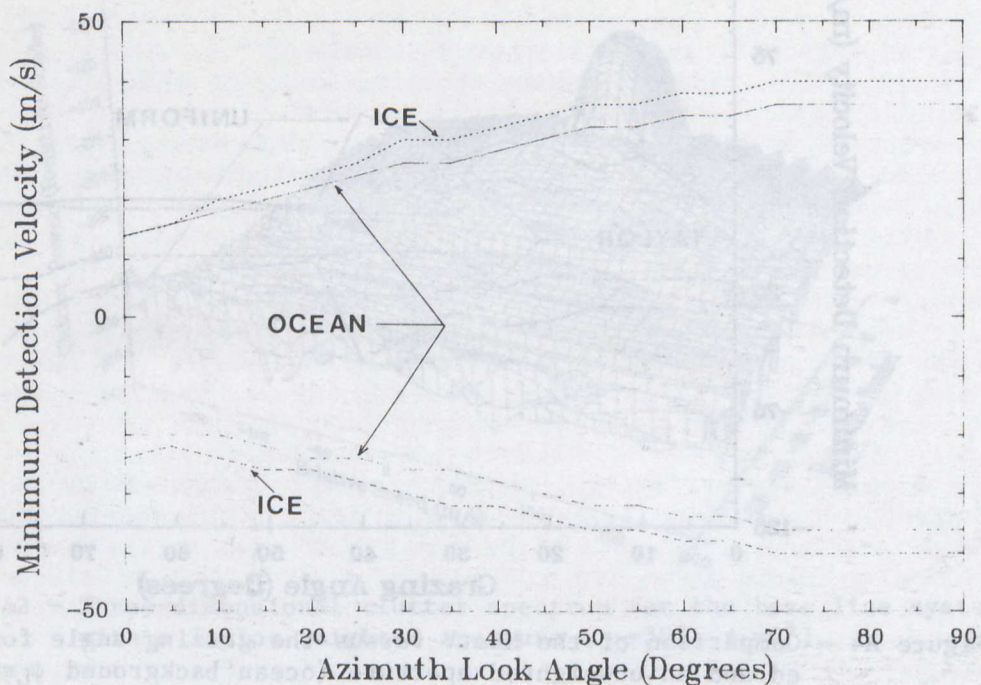Figure A6 – Comparison of the MDetV̄ versus the azimuth look angle for
ice and snow backgrounds using weighted apertures ($\gamma_L=3°$)

DOCUMENT CONTROL DATA – R & D

(Security classification of title, body of abstract and indexing annotation must be entered when the overall document is classified)

1. ORIGINATING ACTIVITY Communications Research Centre P.O. Box 11490, Station H Ottawa, Ontario, K2H 8S2	2a. DOCUMENT SECURITY CLASSIFICATION UNCLASSIFIED 2b. GROUP

3. DOCUMENT TITLE

Analysis of Space-Based Radar Clutter Spectra Over Different Types of Terrain and Their Effects on Detection Performance

4. DESCRIPTIVE NOTES (Type of report and inclusive dates)
CRC Report No. 1408

5. AUTHOR(S) (Last name, first name, middle initial)

FAUBERT, D.,   ROOK, B.J. and TAM, W.

6. DOCUMENT DATE 21 November 1986	7a. TOTAL NO. OF PAGES 42	7b. NO. OF REFS 8
8a. PROJECT OR GRANT NO. 021LA12	9a. ORIGINATOR'S DOCUMENT NUMBER(S)	
8b. CONTRACT NO.	9b. OTHER DOCUMENT NO.(S) (Any other numbers that may be assigned this document)	

10. DISTRIBUTION STATEMENT

Unlimited

11. SUPPLEMENTARY NOTES	12. SPONSORING ACTIVITY Defence Research Establishment Ottawa

13. ABSTRACT

      A computer model was used to make a detailed analysis of the clutter spectra received by real aperture Space-Based Radars orbiting over different types of terrain. The influence of terrain on L-band SBR detection performance has also been studied. It was found that the clutter spectra tend to become narrower as the grazing angle of the antenna increases but that they broaden as the antenna points progressively more away from the direction of motion of the satellite. The interference caused by the clutter background is progressively higher for ice covered ground but smaller for a snow-covered terrain and the smallest for an ocean background. The minimum detectable velocities of the SBR were found to vary by a factor of up to three according to the terrain type.

Security Classification

KEY WORDS

Space-based Radar

Clutter Spectra

Detection Performance

INSTRUCTIONS

1. ORIGINATING ACTIVITY: Enter the name and address of the organization issuing the document.

2a. DOCUMENT SECURITY CLASSIFICATION: Enter the overall security classification of the document including special warning terms whenever applicable.

2b. GROUP: Enter security reclassification group number. The three groups are defined in Appendix 'M' of the DRB Security Regulations.

3. DOCUMENT TITLE: Enter the complete document title in all capital letters. Titles in all cases should be unclassified. If a sufficiently descriptive title cannot be selected without classification, show title classification with the usual one-capital-letter abbreviation in parentheses immediately following the title.

4. DESCRIPTIVE NOTES: Enter the category of document, e.g. technical report, technical note or technical letter. If appropriate, enter the type of document, e.g. interim, progress, summary, annual or final. Give the inclusive dates when a specific reporting period is covered.

5. AUTHOR(S): Enter the name(s) of author(s) as shown on or in the document. Enter last name, first name, middle initial. If military, show rank. The name of the principal author is an absolute minimum requirement.

6. DOCUMENT DATE: Enter the date (month, year) of Establishment approval for publication of the document.

7a. TOTAL NUMBER OF PAGES: The total page count should follow normal pagination procedures, i.e., enter the number of pages containing information.

7b. NUMBER OF REFERENCES: Enter the total number of references cited in the document.

8a. PROJECT OR GRANT NUMBER: If appropriate, enter the applicable research and development project or grant number under which the document was written.

8b. CONTRACT NUMBER: If appropriate, enter the applicable number under which the document was written.

9a. ORIGINATOR'S DOCUMENT NUMBER(S): Enter the official document number by which the document will be identified and controlled by the originating activity. This number must be unique to this document.

9b. OTHER DOCUMENT NUMBER(S): If the document has been assigned any other document numbers (either by the originator or by the sponsor), also enter this number(s).

10. DISTRIBUTION STATEMENT: Enter any limitations on further dissemination of the document, other than those imposed by security classification, using standard statements such as:

   (1) "Qualified requesters may obtain copies of this document from their defence documentation center."

   (2) "Announcement and dissemination of this document is not authorized without prior approval from originating activity."

11. SUPPLEMENTARY NOTES: Use for additional explanatory notes.

12. SPONSORING ACTIVITY: Enter the name of the departmental project office or laboratory sponsoring the research and development. Include address.

13. ABSTRACT: Enter an abstract giving a brief and factual summary of the document, even though it may also appear elsewhere in the body of the document itself. It is highly desirable that the abstract of classified documents be unclassified. Each paragraph of the abstract shall end with an indication of the security classification of the information in the paragraph (unless the document itself is unclassified) represented as (TS), (S), (C), (R); or (U).

   The length of the abstract should be limited to 20 single-spaced standard typewritten lines; 7½ inches long.

14. KEY WORDS: Key words are technically meaningful terms or short phrases that characterize a document and could be helpful in cataloging the document. Key words should be selected so that no security classification is required. Identifiers, such as equipment model designation, trade name, military project code name, geographic location, may be used as key words but will be followed by an indication of technical context.